Collisional modelling of the AU Microscopii debris disc

Ch. Schüppler[1], T. Löhne[1], A. V. Krivov[1], S. Ertel[2], J. P. Marshall[3,4], S. Wolf[5], M. C. Wyatt[6], J.-C. Augereau[7,8], and S. A. Metchev[9]

[1] Astrophysikalisches Institut und Universitätssternwarte, Friedrich-Schiller-Universität Jena, Schillergäßchen 2–3, 07745 Jena, Germany
e-mail: `christian.schueppler@uni-jena.de`
[2] European Southern Observatory, Alonso de Cordova 3107, Vitacura, Casilla 19001, Santiago, Chile
[3] School of Physics, University of New South Wales, NSW 2052 Sydney, Australia
[4] Australian Centre for Astrobiology, University of New South Wales, NSW 2052 Sydney, Australia
[5] Institut für Theoretische Physik und Astrophysik, Christian-Albrechts-Universität zu Kiel, Leibnizstraße 15, 24098 Kiel, Germany
[6] Institute of Astronomy, University of Cambridge, Madingley Road, Cambridge CB3 0HA, UK
[7] Univ. Grenoble Alpes, IPAG, F-38000 Grenoble, France
[8] CNRS, IPAG, F-38000 Grenoble, France
[9] University of Western Ontario, Department of Physics and Astronomy, 1151 Richmond Avenue, London, ON N6A 3K7, Canada

Received June 16, 2015

ABSTRACT

AU Microscopii's debris disc is among the most famous and best-studied debris discs, and one of only two resolved debris discs around M stars. We perform in depth collisional modelling of the AU Mic disc including stellar radiative and corpuscular forces (stellar winds), aiming at a comprehensive understanding of the dust production and the dust and planetesimal dynamics in the system. Our models are compared to a suite of observational data for thermal and scattered light emission, ranging from the ALMA radial surface brightness profile at 1.3 mm to spatially resolved polarisation measurements in the visible. Most of the data are shown to be reproduced with dust production in a belt of planetesimals with an outer edge at around 40 au and subsequent inward transport of dust by stellar winds. A low dynamical excitation of the planetesimals with eccentricities up to 0.03 is preferred. The radial width of the planetesimal belt cannot be constrained tightly. Belts that are 5 au and 17 au wide, as well as a broad 44 au-wide belt are consistent with observations. All models show surface density profiles increasing with distance from the star up to ≈ 40 au, as inferred from observations. The best model is achieved by assuming a stellar mass loss rate that exceeds the solar one by a factor of 50. While the spectral energy distribution and the shape of the ALMA radial profile are well reproduced, the models deviate from the scattered light observations more strongly. The observations show a bluer disc colour and a lower degree of polarisation for projected distances < 40 au than predicted by the models. The problem may be mitigated by irregularly-shaped dust grains which have scattering properties different from the Mie spheres used in this work. From tests with a handful of selected dust materials, we derive a preference for mixtures of silicate, carbon, and ice of moderate porosity. We also address the origin of the unresolved central excess emission detected by ALMA and show that it cannot stem from an additional inner belt alone. Instead, it should derive, at least partly, from the chromosphere of the central star.

Key words. circumstellar matter – stars: individual: AU Mic (GJ 803, HD 197481) – submillimetre: planetary systems – scattering – polarisation – methods: numerical

1. Introduction

Debris discs are remnants of the planet formation process and consist of (unobservable) planetesimals and collisionally replenished dust. They are ubiquitous around main-sequence stars with an incidence rate of about 20% for FGK stars with ages from hundreds of Myr to several Gyr (Eiroa et al. 2013). For $10 - 800$ Myr-old A stars, Su et al. (2006) quoted a higher detection rate of $\approx 30\%$, whereas Thureau et al. (2014) found a similar frequency as for FGK-type stars. The possible difference in the debris disc occurrence rate between the FGK and A stars appears to be largely due to the observed age ranges and the typical disc decay timescale for different spectral types (e.g., Decin et al. 2003; Wyatt et al. 2007; Kains et al. 2011). The frequency of debris discs around M stars remains controversial (Lestrade et al. 2006; Gautier et al. 2007; Forbrich et al. 2008; Plavchan et al. 2009; Lestrade et al. 2009, 2012). Despite the high abundance of M dwarfs in the Galaxy ($\sim 80\%$, Lada 2006), only a few discs around them have been detected so far,

for which several reasons could exist: (i) M dwarfs have low luminosities and are older on average than other stars so that their discs are faint and already mostly collisionally depleted. (ii) The blowout of dust around M stars may be favoured since they likely possess strong stellar winds (e.g., recently Johnstone et al. 2015a,b). (iii) Owing to their low stellar mass, it is easy to strip planetesimals from an M-dwarf disc during close encounters with massive objects. (iv) Debris disc surveys, including stars of various spectral types, reveal generic temperatures for warm and cold disc components of ~ 190 K and ~ 60 K, respectively (Morales et al. 2011; Ballering et al. 2013; Chen et al. 2014). If this also holds for M stars, the M-type discs would be close to the star, meaning a faster dynamic timescale of the disc and a quick depletion of the dust reservoir. Around a dozen of non-resolved M-star discs have been found in the recent years (Forbrich et al. 2008; Plavchan et al. 2009; Chen et al. 2014). Theissen & West (2014) found a much larger number of old M dwarfs showing mid-IR excesses, interpretable as circumstellar dust emission.

1

However, due to the high fractional luminosities measured, the dust is more likely attributed to planetary impacts within the terrestrial zone than to asteroid belt-like debris discs. The discs around the M stars AU Microscopii and GJ 581 (Lestrade et al. 2012) are the only ones that are spatially resolved thus far.

Since the discovery of the AU Mic disc (Kalas et al. 2004; Liu 2004) it remains remarkable among the resolved debris systems in many respects. The disc is seen edge-on with an impressive radial extent of about 150 au and is resolved in the optical to near-IR (Krist et al. 2005; Metchev et al. 2005; Fitzgerald et al. 2007) where it appears blue relative to the star. The surface brightness profiles from the optical/near-IR images show shallow inner slopes at small projected distances but steepen substantially beyond 35 au. In addition, asymmetries on small and large scales with several local brightness maxima and minima have been detected at stellocentric distances beyond 20 au (Liu 2004; Krist et al. 2005; Fitzgerald et al. 2007). In the latest high spatial resolution STIS (Space Telescope Imaging Spectrograph) images, Schneider et al. (2014) found a distinct brightness enhancement above the disc midplane on the south-east (SE) side at about 13 au from the star. Furthermore, a disc warp is discernible on the north-west (NW) side between 13 and 45 au, opposed to the SE brightness bump. There is also an NW-SE asymmetry, with the NW side brighter than the SE side interior to 20 au. These disc inhomogeneities hint at the existence of planetary perturbers, causing radially localised structures such as rings, clumps, and gaps through planet-disc interactions (e.g., Ertel et al. 2012b; Nesvold & Kuchner 2015). However, no confirmation of planets in the AU Mic system is found to date (Neuhäuser et al. 2003; Masciadri et al. 2005; Metchev et al. 2005; Hebb et al. 2007). Alternatively, clumpy disc structures may also be due to recent breakups of large planetesimals (e.g., Kral et al. 2015).

The disc has been also resolved at 1.3 mm with SMA (Submillimetre Array), see Wilner et al. (2012), and with ALMA (Atacama Large Millimetre/submillimetre Array), see MacGregor et al. (2013). From the ALMA observations two distinct emission components have been identified: a dust belt that extends up to 40 au and a central emission peak that remains unresolved. The dust belt shows an emission profile rising with the distance from the star, indicating a steep surface density slope. The central emission peak is ≈ 6 times brighter than the stellar photosphere. MacGregor et al. (2013) surmised this emission stems from an inner planetesimal belt, located $\lesssim 3$ au from the star. Cranmer et al. (2013) proposed it to come solely or partly from an active stellar corona.

This great abundance of available observational data of the AU Mic disc provides valuable information from the smallest up to the largest dust particles, and further to planetesimals that produce the dust through collisional grinding. Constraints on the properties and spatial distribution of (sub)micron-sized particles can be inferred from the short-wavelength observations where the dust's scattered light is detected. However in the AU Mic edge-on system, this is impeded by the degeneracy between the scattering properties of grains and their supposed spatial distribution, and requires a good knowledge of the phase and polarisation function of small dust. The dynamics of small particles is strongly affected by radiative and corpuscular forces, resulting in radiative or stellar wind blowout and drag, depending on the grain and stellar properties. Observations at longer wavelengths show the thermal emission of larger grains and give insights into their spatial distribution. Especially, resolved images in the radio range reveal the locations of mm-sized, tracing the underlying parent bodies (planetesimals).

Much work has been done in the past to characterise and model the AU Mic system. Augereau & Beust (2006) performed a direct inversion of the visible and near-IR surface brightness profiles. From H-band observations a disc surface number density was obtained that peaks around 35 au, close to the location of the break in the brightness profile, which hints at a planetesimal belt around that distance. Furthermore, by fitting the blue disc colour they constrained the grain size distribution and found that grains smaller than 1 μm are mandatory to explain the observations. The study of Strubbe & Chiang (2006) included the dynamics of grains for the first time. There, a narrow birth ring of planetesimals at about 40 au was assumed. Micron-sized dust grains are produced through mutual collisions of the birth-ring objects. Grains with sizes < 1 μm that are smaller than the radiative and corpuscular blowout limit, are expelled from the system by direct radiation and stellar wind pressure. Slightly larger grains are either barely bound and launched into eccentric orbits, hence forming a halo, or are transported into the inner regions of the system by Poynting-Robertson and stellar wind drag. The largest grains follow the dynamics of their parents and remain in the birth ring. Strubbe & Chiang concluded that the disc is collision dominated with an inner part devoid of submicron-sized grains (consistent with polarisation measurements of Graham et al. 2007), and small grains mainly populate the outer part of the disc, causing the blue colour of the scattered light. Fitzgerald et al. (2007) attempted to simultaneously reproduce the scattered light profiles, the degree of polarisation, and the spectral energy distribution (SED) with a two-zone disc, using power-law descriptions for the radial and size distribution of the dust in each zone. They showed that the first zone (35 – 40 au) of large particles, representative for a planetesimal ring, mainly accounts for the long-wavelength thermal emission, whereas the second zone (40 – 300 au), composed of small particles, well reproduces the scattered light measurements. Recently, a dust halo was also detected in far-IR resolved *Herschel* and JCMT (James Clerk Maxwell Telescope) images by Matthews et al. (in prep.). Their best fit supports the narrow birth-ring model of Strubbe & Chiang (2006), but is also consistent with an extended planetesimal ring from 8 – 40 au, according to the model explored in Wilner et al. (2012) and MacGregor et al. (2013).

In this study, we undertake collisional modelling to find a generic size and radial distribution of the dust in the AU Mic disc. We aim at a comprehensive understanding of the dust production and the dust and planetesimal dynamics in this system. For the first time, we combine constraints from scattered light and mm wavelength observations and search for a self-consistent collisional model that explains all these data. We assume an axisymmetric disc, and therefore do not account for the formation of substructures and asymmetries observed in the AU Mic disc. Section 2 gives an overview of the observational data and presents our re-reduction of the ALMA data, resulting in a star+disc flux density and a radial surface brightness profile at 1.3 mm. Section 3 explains our collisional model. Section 4 shows the modelling of the extended, ≈ 40 au-wide emission zone, seen in the ALMA image, which we refer to as resolved outer disc. Section 5 addresses a possible origin of the unresolved central emission. In Sect. 6, we compare our results from collisional modelling with a multidimensional power-law fitting approach. Conclusions are drawn in Sect. 7.

2. Data used

2.1. Stellar properties

AU Mic (GJ 803, HD 197481) is an M1 V dwarf at a distance of 9.9 pc (Perryman et al. 1997; van Leeuwen 2007). The star is a bright X-ray and UV emitter and shows strong flaring activity (e.g., Robinson et al. 2001). We used the photosphere model of Augereau & Beust (2006) with an effective temperature of 3700 K, a luminosity of $0.09\,L_\odot$, and a surface gravity of $\log(g) = 4.5$ (CGS). We assumed a stellar mass of $0.5\,M_\odot$, motivated by the mean of the wide mass range given in the literature ($0.3 - 0.6\,M_\odot$, Plavchan et al. 2009; Houdebine & Doyle 1994). Note that this assumption is roughly consistent with the photosphere model used that predicts $\approx 0.6\,M_\odot$.

AU Mic belongs to the β Pic moving group (BPMG) and its age coincides with the BPMG age by assuming a coeval origin of all group members. Through the identification of the lithium depletion boundary, Binks & Jeffries (2014) and Malo et al. (2014) found BPMG ages of 21 ± 4 Myr and 26 ± 3 Myr, respectively. This agrees with traceback ages from Makarov (2007) and Mamajek & Bell (2014). The latter used revised *Hipparcos* astrometry data and also derived an isochronal age of 22 ± 3 Myr.

2.2. ALMA observations

ALMA observations of AU Mic in Band 6 (1.3 mm) have been carried out as part of the cycle 0 early science observations in the context of the projects 2011.0.00142.S (PI: D. Wilner) and 2011.0.00274.S (PI: S. Ertel). The data considered in the present work were taken on 16 June 2012 and are in agreement with the MacGregor et al. (2013)'s SB-4 observations. A total of 20 operational 12-m antennae were used, spanning baselines of $21 - 402$ m with an effective angular resolution (*FWHM* of the reconstructed dirty beam) of $0.69'' \times 0.79''$ and an effective field of view of $\lambda/D \approx 22''$ (with λ the observing wavelength and D the single dish diameter). MacGregor et al. (2013) presented a detailed description of the observations and data reduction. Our re-reduction of the data was carried out in the Common Astronomy Software Applications (CASA, McMullin et al. 2007). We followed the approach used by MacGregor et al. (2013) and came to consistent conclusions.

The edge-on disc has a radial extent of about $4''$ (≈ 40 au) and a position angle of $128.41 \pm 0.13°$ (MacGregor et al. 2013). It is unresolved in its vertical direction. We refrain from presenting the ALMA image as it would not provide information beyond that shown in Fig. 1 of MacGregor et al. (2013). In order to prepare the data for our modelling, we extracted a radial profile along the disc major axis. To this end, we largely adopted the approach used for *Herschel* data obtained in the context of the Open Time Key Programme DUst around NEarby Stars (DUNES, Löhne et al. 2012; Eiroa et al. 2013; Ertel et al. 2014). We first converted the flux units in the image from Jy/beam to Jy/pixel by multiplying them with a factor of 0.0185 derived by integrating the core of the reconstructed dirty beam. Then, we rebinned the image with an original pixel scale of $0.1''$/pixel to a ten times smaller pixel scale using a cubic spline interpolation and rotated it by an angle of $38.41°$ clockwise in order to align the disc major axis with the image x-axis. From this image, we measured the radial profile along the disc major axis by integrating over 11×11 subpixel-wide boxes centred on the disc midplane and spaced by 74 subpixels ($0.74''$, about the *FWHM* of the reconstructed dirty beam, i.e. the resolution element of the image) left and right of the star, assumed to be located at the brightest subpixel. We averaged the SE and NW sides of the profile to fit an axisymmetric model to the data. Uncertainties were derived as a quadratic sum of the difference between the two sides of the profile and the background fluctuation measured in regions of the image where no flux is expected but where the sensitivity is comparable to the image centre. As we were only interested in the dust distribution in the outer disc, we ignored the profile point at the image centre, which is affected by the inner, unresolved component. By extrapolating the disc profile from the outer points to the disc centre and assuming that the flux measured above the extrapolated value stems from the inner component (star and additional emission), we estimated a flux density of this component of 0.29 ± 0.05 mJy, consistent with 0.36 ± 0.07 mJy in MacGregor et al. (2013). We estimated the uncertainty of this measurement by adding in quadrature a typical uncertainty in the outer points ($\sim 15\%$) and an absolute photometric calibration uncertainty of 10% (MacGregor et al. 2013). The stellar contribution to this flux density is 0.04 mJy, obtained from the stellar photosphere spectrum (Augereau & Beust 2006) extrapolated to the ALMA wavelength using the Rayleigh-Jeans law. However, this might significantly underestimate the stellar flux and the whole central component might originate from stellar emission (Cranmer et al. 2013).

Deviating from the complex fitting approach used by MacGregor et al. (2013) to derive the disc parameters (including the total flux density), we performed photometry of the disc by integrating the flux in the rotated image in a box of 101×21 native image pixels. The uncertainty was estimated from the scatter of the flux measured on eight positions above and below the disc, where no emission is expected. An additional calibration uncertainty of 10%, consistent with MacGregor et al. (2013), was added in quadrature. We found a total flux density of 8.75 ± 0.98 mJy, which is consistent with 7.46 ± 0.76 mJy from MacGregor et al. (2013), by summing both disc components and including calibration uncertainty. For the modelling, we subtracted the flux of the inner component estimated above, so that we are left only with the flux of the disc and the star as estimated using our photosphere spectrum.

Note that the exact flux of the inner component has no significant impact on our profile or flux measurement, since we ignore the inner profile point affected by this component and because its contribution to the total flux density is only 0.2σ.

2.3. Auxiliary data

In addition to the ALMA data, we considered for modelling a variety of photometric data from earlier work. Furthermore, we included archival *Herschel* (Pilbratt et al. 2010) PACS (Photodetector Array Camera and Spectrometer, Poglitsch et al. 2010) and SPIRE (Spectral and Photometric Imaging Receiver, Griffin et al. 2010; Swinyard et al. 2010) data, obtained in the context of the debris disc Guaranteed Time Observations programme (PI: G. Olofsson, see Matthews et al., in prep.). These data were treated following the *Herschel*/DUNES data reduction strategy (Eiroa et al. 2013). HIPE (*Herschel* Interactive Processing Environment, Ott 2010) version 11 and the calibration plan versions v56 and v11 for PACS and SPIRE, respectively, were used. PACS flux densities at $70\,\mu m$ and $160\,\mu m$ were measured with an aperture of $20''$ and annuli for the noise measurement of $30 - 40''$ and $40 - 60''$, respectively. The SPIRE flux density at $250\,\mu m$ was measured with an aperture of $30''$ and the noise was estimated in a region of the image where no emission from the disc is expected. A nearby source is visible in all *Herschel* images, peaking at $250\,\mu m$. It is well separated

from the disc at wavelengths up to 250 μm and easily removed by a point source subtraction. The two sources are not well separated at longer wavelengths. SPIRE flux densities at 350 μm and 500 μm were measured using SExtractor (Bertin & Arnouts 1996) and a point source approximation (PSF photometry), since the source is unresolved at these wavelengths. Aperture corrections were applied to the measured fluxes. Instrument calibration uncertainties of 7% for PACS and 6% for SPIRE were added in quadrature to the measured uncertainty. Note that a more detailed reduction of the *Herschel* data will be given in Matthews et al. (in prep.). Minor differences to the data used here exist, but all within 2σ (B. Matthews, priv. comm.). The differences have no impact on the results presented in this work.

We did not consider the spatially resolved information from the *Herschel* images since the resolution is much lower than that of our ALMA image (e.g., $FWHM = 5.8''$ for *Herschel*/PACS at 70 μm vs. $FWHM = 0.74''$ for ALMA Band 6). However, we inspected the PACS data for signs of bright, warm central emission in the form of a significantly increasing extent of the disc from 70 μm to 160 μm (Ertel et al. 2014). Such a behaviour is not visible suggesting that the inner component seen in the ALMA images has indeed no or only a minor contribution to the fluxes at shorter wavelengths. Doering et al. (2005) reported a detection of the innermost disc regions up to ≈ 16 au in diameter via *N*-band imaging at Gemini South. However, only a low-level surface brightness extension along the direction of the edge-on disc was found that has not been taken into account in our study. Furthermore, we did not consider *Spitzer*/MIPS images due to the low angular resolution (e.g., the resolution of Spitzer at 24 μm is nearly as low as that of *Herschel* at 70 μm). Any confusion, e.g. from a background galaxy, would here be difficult to disentangle from the source.

Assuming the flux density to be proportional to $\lambda^{-\delta}$ at long wavelengths, the mean spectral index beyond 250 μm amounts to $\delta = 1.7$, close to the Rayleigh-Jeans (RJ) slope of a blackbody radiator ($\delta_{RJ} = 2$). We fitted a blackbody curve to the far-IR excess in order to derive spectral slopes at all wavelengths. A temperature of 50 K fits the data very well, consistent with Rebull et al. (2008) and Plavchan et al. (2009). Interestingly, this is close to the generic temperature found for the outer cold components in many two-component disc systems (Morales et al. 2011; Ballering et al. 2013; Chen et al. 2014; Pawellek et al. 2014). The temperature that was found for the inner disc, 190 K, corresponds to a very small distance of 0.7 au for a putative warm component in the AU Mic system. This is well below the resolution limit and leaves room for further speculations about the presence of an inner unresolved disc component. We took the nearest tabulated values for the colour corrections listed in the literature for the instruments used and the spectral slopes of the source (star and disc) derived from this fit. The resulting colour corrected flux densities and references for both the measurement and the colour correction are listed in Table 1.

2.4. Scattered light

The AU Mic disc is 60% brighter in *B*-band than in *I*-band relative to the star (Krist et al. 2005). A potential explanation is a significant amount of small grains that scatter more light at shorter wavelengths. Augereau & Beust (2006) constrained the grain size distribution by fitting the blue disc colour. They concluded that grains down to ~ 0.1 μm are necessary to explain the observations when astronomical silicate or graphite grains are assumed. Graham et al. (2007) obtained polarisation maps in *V*-band using the *Hubble Space Telescope* (HST) Advanced

Table 1. Colour-corrected photometry of AU Mic.

Wavelength [μm]	Flux density [mJy]	Telescope/ Instrument	Ref. Flux	Ref. Col. corr.
3.35	4820 ± 119	WISE	C12, W10	W10
4.6	4260 ± 119	WISE	C12, W10	W10
5.8	2200 ± 55	*Spitzer*/IRAC	C05	IH
8	1270 ± 20	*Spitzer*/IRAC	C05	IH
9	912 ± 22	Akari	I10	IH
11.6	543 ± 60	WISE	C12	W10
12	517 ± 30	IRAS	M90	B88
18	246 ± 36	Akari	I10	IH
22.1	183 ± 21	WISE	C12	W10
24	158 ± 3	*Spitzer*/MIPS	P09	IH
25	244 ± 63	IRAS	M90	B88
60	269 ± 46	IRAS	M90	B88
70	227 ± 27	*Spitzer*/MIPS	P09	IH
70	231 ± 16	*Herschel*/PACS	HSA	IH
100	680 ± 149	IRAS	M90	B88
160	172 ± 21	*Spitzer*/MIPS	R08	IH
160	243 ± 17	*Herschel*/PACS	HSA	IH
250	134 ± 8	*Herschel*/SPIRE	HSA	IH
350	72 ± 21	CSO/SHARCII	C05	...
350	84.4 ± 5.4	*Herschel*/SPIRE	HSA	IH
450	85 ± 42	JCMT/SCUBA	L04	...
500	47.6 ± 3.8	*Herschel*/SPIRE	HSA	IH
850	14.4 ± 1.8	JCMT/SCUBA	L04	...
1300	8.5 ± 2.0	SMA	W12	...
1300	8.75 ± 0.98	ALMA	M13	...

References. B88: Beichman et al. (1988), C05: Chen et al. (2005), C12: Cutri & et al. (2012), HSA: *Herschel* Science Archive (Matthews et al., in prep.). IH: corresponding instrument hand book. I10: Ishihara et al. (2010), L04: Liu et al. (2004), M90: Moshir et al. (1990), M13: MacGregor et al. (2013), P09: Plavchan et al. (2009), R08: Rebull et al. (2008), W10: Wright et al. (2010), W12: Wilner et al. (2012). The ALMA and *Herschel* data were re-analysed in the present work.

Camera for Surveys. They measured the degree of linear polarisation to be steeply rising from 5 to 40% within a distance of 80 au from the star. The light is polarised perpendicular to the disc plane that agrees with the expected scattering behaviour by small grains with size parameters $x \lesssim 1$ (equivalent to typical grain sizes < 1 μm). To model the *V*-band scattered light intensity and the degree of polarisation, Graham et al. (2007) assumed uniformly distributed dust between two distances from the star and adopted the empirical Henyey & Greenstein (1941) phase function in combination with a parameterized polarisation function. In their best-fit model, the particles exhibit strong forward scattering and the innermost 40 au of the disc are devoid of grains. Later on, Shen et al. (2009) showed that the results from Graham et al. (2007) can be reproduced by a distribution of sphere cluster aggregates with size distribution index -3.5, volume-equivalent radii between 0.1 and 0.4 μm, and a porosity of 60%.

In this work, our models are compared with the optical and near-IR surface brightness profiles from Fitzgerald et al. (2007) and Schneider et al. (2014) and with the measured degree of polarisation from Graham et al. (2007). As our modelling deals with axisymmetric discs, all observed profiles had been averaged over the SE and NW disc sides in order to remove the observed surface brightness anomalies.

2.5. Gas in the disc

Some studies searched for circumstellar gas in the AU Mic disc. From a non-detection of submillimetre CO emission Liu et al. (2004) inferred an H_2 mass of $\leq 1.3\,M_\oplus$. Roberge et al. (2005) reduced the H_2 mass limit to $0.07\,M_\oplus$ due to a non-detection of far-UV H_2 absorption. France et al. (2007) analysed fluorescent H_2 emission and found a total gas mass between $4 \times 10^{-4}\,M_\oplus$ and $6 \times 10^{-6}\,M_\oplus$, but stated that this detection might also come from a cloud that extends beyond the disc. From X-ray spectroscopy Schneider & Schmitt (2010) reported a maximum H column density of $\sim 10^{19}\,cm^{-2}$, which is about five times higher than the interstellar value. However, since observational data point towards a very low gas content in the AU Mic disc, we neglect the influence of any gas in our investigations.

3. Collisional modelling

Collisional modelling with our code ACE (Analysis of Collisional Evolution) and its application to debris disc systems is described extensively in previous papers (Krivov et al. 2006, 2008; Müller et al. 2010; Reidemeister et al. 2011; Löhne et al. 2012; Krivov et al. 2013; Schüppler et al. 2014, among others). The code assumes a disc of planetesimals orbiting a central star, simulates their collisional grinding, and follows the collisional and dynamical evolution of the system under a variety of physical effects. ACE works with a three-dimensional logarithmic grid for objects mass, pericentric distance, and eccentricity. The simulations consider a number of parameters, including those that define the initial distribution of planetesimals, the strength of particle transport, and material properties such as the critical fragmentation energy. The following sections detail the parameters chosen in our modelling.

3.1. Stellar winds and mass loss rate

Stellar winds (SW) are expected to play a crucial role in discs around late-type stars such as AU Mic where they are typically stronger than for early-type stars (e.g., Plavchan et al. 2005, 2009; Strubbe & Chiang 2006; Reidemeister et al. 2011; Schüppler et al. 2014). The total stellar wind force that acts on the circumstellar dust can be decomposed to direct stellar wind pressure, which is directed radially outwards, and stellar wind drag, which works like a headwind on the particles that causes them to gradually lose orbital energy and angular momentum, and therefore, to spiral inwards (Burns et al. 1979). Depending on the stellar wind strengths and the size of the particles they are interacting with, the result could be either a grain transport towards the star or a blowout of smaller grains from the system.

Previous studies proposed various stellar winds strengths for the AU Mic system, expressed in terms of multiples of the solar mass loss rate, $\dot{M}_\odot = 2 \times 10^{-14}\,M_\odot\,yr^{-1}$. Strubbe & Chiang (2006) constrained the stellar mass loss rate to be $\dot{M}_\star < 10\,\dot{M}_\odot$ which was in good agreement with the observed SED and the $V - H$ colour profile of the disc. This relatively weak wind strength means that the disc is rather dominated by destructive grain-grain collisions than transport processes. Plavchan et al. (2009) estimated $\dot{M}_\star < 50\,\dot{M}_\odot$ from considerations of *Spitzer*/IRS observations. Augereau & Beust (2006) took into account the active nature of AU Mic, and found $\dot{M}_\star \approx 50\,\dot{M}_\odot$ during quiescent states and $\dot{M}_\star \approx 2500\,\dot{M}_\odot$ during flares. The star spends about 10% of the time in flare phases with typical flare durations of several minutes (Pagano et al. 2000). Averaging over quiescent and flare phases yields a mean stellar

mass loss of $\dot{M}_\star = 300\,\dot{M}_\odot$. This high wind strength means that the direct stellar wind pressure is larger than the radiation pressure which causes an efficient transport of small dust into outer disc regions.

In our modelling, we considered moderate and strong wind strengths by assuming $50\,\dot{M}_\odot$ and $300\,\dot{M}_\odot$. Throughout this paper, we refer to both cases as SW50 and SW300. According to Augereau & Beust (2006), SW50 is a typical model where the flares are ignored, while SW300 is an attempt to account for the impact of the episodic stellar activity. In all simulations involving stellar winds, we used Eq. (7) of Gustafson (1994) for the total stellar wind force acting on a particle and assumed a wind speed $v_{sw} = 400\,km\,s^{-1}$ (Strubbe & Chiang 2006).

3.2. Grain material

Graham et al. (2007) and Fitzgerald et al. (2007) found evidence for porous aggregates containing silicate, carbon, and ice. Guided by these results, we used porous grains composed of astronomical silicate (Draine 2003), ACH2 amorphous carbon (Zubko et al. 1996), and water ice (Li & Greenberg 1998). Since the ACH2 refractive data from Zubko et al. (1996) terminate at $\lambda \approx 1\,mm$ and do not cover the full wavelength range for all available photometric measurements, we extrapolated the real and imaginary parts up to $\lambda = 2\,mm$ by the function $c_1\,(\lambda/1\,mm)^{c_2}$. The extrapolation gives $(c_1, c_2) = (16.2, 0.27)$ and $(c_1, c_2) = (5.6, -0.26)$ for real and imaginary parts, respectively.

We generated different porous silicate-carbon-ice mixtures and calculated the refractive indexes of the composites by applying the Bruggeman (1935) mixing rule. The materials considered in this study are given in Table 2. For brevity, we use the identifiers M1 to M5 when referring to the different compositions.

Table 2. Materials used for modelling.

Name	Composition	Density [$g\,cm^{-3}$]	Blowout size [μm] SW50	SW300
M1	sil33+car33+vac33	1.78	0.07	0.48
M2	sil50+car50	2.68	0.04	0.35
M3	sil25+car25+ice25+vac25	1.64	0.07	0.51
M4	sil10+car10+ice40+vac40	1.02	0.11	0.71
M5	sil15+car15+vac70	0.80	0.16	0.93

Notes. Numbers after material names denote their volume fraction in percent, e.g. sil25+car25+ice25+vac25 = 25% silicates + 25% carbon + 25% ice + 25% vacuum. The bulk densities of the composites are given by $\rho_{mix} = \sum \rho_i\,\sigma_i$, where σ_i denotes the volume fraction of the species, and ρ_i their densities ($\rho_{sil} = 3.5\,g\,cm^{-3}$, $\rho_{car} = 1.85\,g\,cm^{-3}$, $\rho_{ice} = 1.2\,g\,cm^{-3}$). Blowout sizes are grain radii for which β equals 0.5 (see text).

We assumed spherical dust grains. Each grain has a certain radius s which is denoted as its size. Optical properties of the grains were determined by means of Mie theory (Bohren & Huffman 1983). Figure 1 shows $\beta = \beta_{rad} + \beta_{sw} = F_{rad}/F_{grav} + F_{sw}/F_{grav}$, the ratio of direct radiation and direct stellar wind pressure forces to stellar gravity (Burns et al. 1979) as a function of grain size. A detailed description of β_{sw} includes a dependency on the distance from the star, r, due to radial variations of the stellar wind velocity.
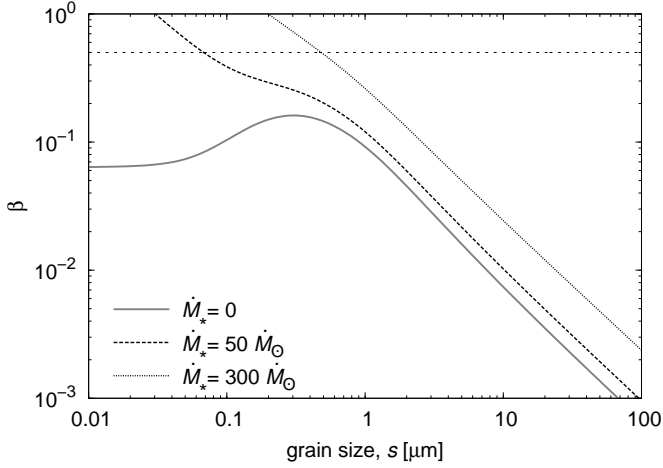
Fig. 1. β-ratio for different assumptions of AU Mic's stellar mass loss rate $\dot{M}_\star$. The material consists of 33% carbon, 33% silicate, and 33% vacuum (M1). The horizontal dashed line depicts $\beta = 0.5$. Particles with $\beta > 0.5$ are ejected from the system owing to radiation and stellar wind pressure.

However, this effect is weak for $r > 15$ au (Augereau & Beust 2006) and we considered β_{sw} independent of r. Further, we assumed the reflection of wind particles on the surface of the dust grains that means an efficiency of momentum coupling of $C_D = 2$ (Gustafson 1994).

The orbits of the collisionally-produced dust grains become more and more eccentric with increasing β. For $\beta > 0.5$, the grains get eccentricities > 1 and are expelled from the system on hyperbolic orbits if they are released from bodies on circular orbits. As a measure for the blowout size, we define $s_{blow} = s(\beta = 0.5)$. However, when particles are released from eccentric orbits, the blowout occurs between $\beta = (1-e)/2$ at the periastron and $(1 + e)/2$ at the apastron (Burns et al. 1979), where e is the typical eccentricity of the parent bodies that eject the dust. ACE computes the orbital elements of the fragments depending on the masses, semi-major axes, eccentricities, and β's of the colliding bodies, and thus, automatically accounts for bound and unbound grains launched from non-circular orbits (Krivov et al. 2006). Therefore, the minimum size of *bound* grains in the debris disc system is slightly smaller than s_{blow}. Nevertheless, we found this effect to be small and s_{blow} can be considered a representative value for the minimum grain size.

In the case of weak or no stellar winds, β is smaller than the blowout limit 0.5 for all grain sizes (see Fig. 1, $\dot{M}_\star = 0$). With increasing stellar wind strength the dust particles experience a stronger radial wind pressure. Assuming a radiation pressure efficiency $Q_{pr} = 1$ (Burns et al. 1979), yields $F_{sw}/F_{rad} \sim 0.5$ for SW50 and $F_{sw}/F_{rad} \sim 3$ for SW300. As a result, if the stellar winds are sufficiently strong, the β-ratio that would otherwise be smaller than 0.5 can exceed this critical value at the smallest dust sizes. This defines a blowout size, terminating the lower end of the size distribution (Table 2). Note that Fig. 1 shows β for M1 exemplarily. The other materials given in Table 2 follow a similar dependence of β on size.

The mechanical strength of the materials was defined by a modified version of the Benz & Asphaug (1999) description of the critical energy for fragmentation and dispersal,

$$Q_D^\star = \left[Q_{D,s} \left(\frac{s}{1\,\text{m}} \right)^{b_s} + Q_{D,g} \left(\frac{s}{1\,\text{km}} \right)^{b_g} \right] \left(\frac{v_{imp}}{3\,\text{km s}^{-1}} \right)^\kappa, \quad (1)$$

where $(Q_{D,s}, b_s)$ and $(Q_{D,g}, b_g)$ are two pairs of constants, characterising the strength and gravity regime, respectively, and v_{imp} denotes the impact speed. $Q_D^\star$ is the impact energy per unit target mass necessary to disperse the target into fragments where the largest fragment disperses at most half of the original target mass. For objects smaller than 100 m, $Q_D^\star$ is mainly determined by the material strength, while for larger sizes the gravitational binding energy dominates. The material strength also depends on the material composition, but this dependence is still insufficiently constrained by laboratory work. Therefore, we used the same $Q_D^\star$ for all materials given in Table 2 and assumed $Q_{D,s} = Q_{D,g} = 5 \times 10^6$ erg g^{-1}, $b_s = -0.37$, $b_g = 1.38$, and $\kappa = 0.5$ (Löhne et al. 2012, and references therein).

3.3. Setup

Table 3 lists all ACE simulations discussed in this paper. We distinguish between three disc types, named by the width and location of their planetesimal belt (PB): (i) a narrow outer PB; (ii) a radially extended PB, and (iii) a narrow inner PB. Configurations (i) and (ii) describe models for the outer resolved disc, whereas (iii) corresponds to a model for the central emission seen by ALMA. In all simulations, we assumed the discs to be composed of planetesimals up to at least 10 m in radius with an initial size distribution $\propto s^{-3.5}$. The planetesimals are large enough to ensure that their collisional lifetime is longer than the time needed to reach a quasi-steady state material distribution at dust sizes (Löhne et al. 2008). Thus, the results of the simulations are independent of the maximum size of the objects. The code also accounts for cratering and bouncing collisions where the bulk of one or both colliders stays intact but fragments are released. For each collision, the distribution of fragments is assumed to follow a power law with a mass distribution index -1.83 down to the smallest objects represented in the grid. The planetesimal discs were assumed to be stirred to a maximum eccentricity, e_{max}. The bodies in the disc were assumed to be uniformly distributed within a semi-opening angle $i_{max} = e_{max}/2$ (energy equipartition). After reaching a quasi-steady state, each simulation was evolved until the dust mass had reduced sufficiently to reproduce the observed excess emission. In general, the simulation time, t_{sim}, does not coincide with the physical age, $t_{phys} \approx 20-30$ Myr, of the AU Mic system. For all models except the one with planetesimals between 1 and 45 au, t_{sim} was 2 to 4 times shorter than t_{phys}. These times are more than enough to bring the model discs to collisional equilibrium. The initial conditions of our model discs are, however, fiducial. Different combinations of total initial mass and initial size distribution can lead to the same observed dust configuration, though after different times. An estimate for the minimal initial disc mass necessary to provide the observed amount of dust after t_{phys} can be obtained by assuming that the collisional lifetimes, t_{col}, of the largest bodies equal the system age, enabling them to sustain sufficient dust production over that time. The required sizes for the largest bodies, s'_{max}, typically exceed those in our simulation runs. We extrapolated the size distributions and collisional lifetimes to derive s'_{max} such that $t_{col}(s'_{max}) \approx t_{phys}$, and then, determined the minimum initial disc masses M_{min} for particle sizes up to s'_{max}. The power-law distributions in the m-to-km size range facilitate that extrapolation. The results are listed in Table 3. These masses reflect the minimum disc masses necessary to achieve simulation times that would approach t_{phys}. Larger planetesimals and potential exo-Plutos cannot be assessed this way because their direct contributions to the collisional cascade are negligible.

Table 3. Description of ACE runs.

Disc type	Extent[a] [au]	r-distr.[b]	$\dot{M}_\star$[c] [$\dot{M}_\odot$]	e_{max}[d]	i_{max}[e] [rad]	Material[f]	M_d[g] [$M_\oplus$]	s'_{max}[h] [m]	M_{min}[i] [$M_\oplus$]	Grid resol.[j]	Sect.[k]
narrow outer PB	37.5 – 42.5	$\propto r^0$	0	0.03	0.015	M1	1.5×10^{-3}	20	0.02	m1,e1,p1	4.1
			50				1.7×10^{-3}	100	0.05		
			300				2.1×10^{-3}	250	0.1		
	37.5 – 42.5	$\propto r^0$	50	0.03	0.015	M2	2.4×10^{-3}	100	0.06	m1,e1,p1	4.2
						M3	1.5×10^{-3}	100	0.05		
						M4	1.4×10^{-3}	200	0.05		
	37.5 – 42.5	$\propto r^0$	50	0.01	0.005	M1	1.7×10^{-3}	30	0.05	m1,e1,p1	4.3
				0.1	0.05		6.4×10^{-4}	100	0.03		
extended outer PB	25.5 – 42.5	$\propto r^0$	50	0.03	0.015	M1	1.7×10^{-3}	100	0.08	m1,e1,p1	4.4
	1.0 – 45	$\propto r^{-1.5}$					2.1×10^{-3}	100	0.2	m2,e1,p1	
narrow inner PB	2.8 – 3.2	$\propto r^0$	50	0.03	0.015	M1	6.2×10^{-6}	1×10^5	0.02	m1,e1,p2	5
						M3	5.4×10^{-6}	4×10^5	0.02		
						M5	4.5×10^{-6}	4×10^5	0.02		

Notes. [a] Radial extent of the planetesimal belt; [b] Specification of the radial distribution of planetesimals; [c] Stellar mass loss rate in units of the solar value; [d] Maximum eccentricity of the planetesimal orbits; [e] Semi-opening angle of the planetesimal disc; [f] Name of dust material used (symbol explanation in Table 2); [g] Derived dust mass (grains up to 1 mm in radius); [h] Object size for which the collisional lifetime equals the physical age of the AU Mic system; [i] Estimated minimum total disc mass (grains up to size s'_{max}); [j] Specification of grid: 37 bins in mass from 5×10^{-18} to 1×10^{10} g (m1), 40 bins in mass from 8×10^{-18} to 1×10^{13} g (m2), 22 bins in eccentricity from 0.001 to 2 (e2), 30 bins in pericentric distance from 1 to 60 au (p1), 20 bins in pericentric distance from 0.1 to 7 au (p2); [k] Section number in this work where the runs are addressed.

4. Resolved outer disc

First, we seek to explain the available observational data on the resolved outer AU Mic disc, including the SED, the ALMA radial brightness profile, and scattered light measurements. In the following, we present several modelling attempts, illustrating the influence of different parameters and their compatibility with the data. We start with an investigation of the stellar wind strength to find an appropriate reference run (Sect. 4.1). In a subsequent analysis (Sects. 4.2, 4.3, and 4.4), we vary other initial disc parameters of this reference run in order to more tightly constrain the parameters and reveal degeneracies among them.

4.1. Stellar wind strength

In a first step, we sought after a reasonable assumption for the stellar wind strength and carried out the runs SW0, SW50, and SW300. SW0 does not assume any stellar wind activity at all ($\dot{M}_\star = 0$). Here, the transport of particles is controlled by Poynting-Robertson drag only. In SW50 and SW300, moderate and extreme stellar winds are considered, given by 50 times and 300 times the solar strength, respectively (see Sect. 3.1 for justification of these values).

For other disc parameters, we took reasonable values that have been preferred by previous studies. Inspired by the birthring scenario of Strubbe & Chiang (2006), we assumed a radially narrow planetesimal belt centred at a stellocentric distance $r_{PB} = 40$ au, having the full width $\Delta r_{PB} = 5$ au. In all three runs, the maximum eccentricity of the planetesimals was set to $e_{max} = 0.03$, motivated by Löhne et al. (2012) and Schüppler et al. (2014) who showed a preference for low dynamical excitations in debris discs around late-type stars. For the grain material, we chose a homogeneous mixture with volume filled in equal parts by astronomical silicate, amorphous carbon, and vacuum, denoted as M1 (Table 2). Other assumptions for the

material composition, e_{max}, and Δr_{PB} are probed in the Sects. 4.2, 4.3, and 4.4.

4.1.1. Impact on thermal emission

Figure 2 shows SEDs and normal optical thicknesses, $\tau_\perp$, for SW0, SW50, and SW300. The vertical height of each SED was fitted by searching for the timestep in the ACE simulations where the dust mass has an appropriate value to reproduce the observed level of thermal emission. For the SEDs, we determined χ^2_{SED}/N, which is the sum of the squares of the deviations of our models from N individual photometric points, divided by N. To this end, we considered the $N = 20$ SED points for $\lambda > 10\,\mu m$ (Table 1). We stress that the models are not fitted to the data through variations of the initial disc parameters. The χ^2_{SED}/N metric merely serves for a better comparison of the SED models. All models show good fidelity with the photometry between $160 - 850\,\mu m$ but markedly underestimate or tend to underestimate the 1.3 mm data. At shorter wavelengths, SW50 provides a good match to the data, whereas SW0 significantly underestimates the mid-IR points and SW300 the 70 μm point.

In the planetesimal zone of run SW0, the amount of particles continuously increases with decreasing grain size apart from an underabundance around $s = 0.4\,\mu m$ (Fig. 2d, $r = 39$ au). Although the smallest grains in the range of a few tens of microns are the most frequent, they barely affect the SED as their thermal emission is negligible in the IR. Thus, the effective minimum grain size is given by the maximum of the size distribution at around 10 μm. This large grain size is characteristic for discs with low dynamical excitation of the planetesimals (Thébault & Wu 2008; Löhne et al. 2012; Krivov et al. 2013; Schüppler et al. 2014). The size distributions in SW50 and SW300 show maxima near 0.07 μm and 0.5 μm, respectively (Fig. 2e,f). These values are close to the blowout sizes, s_{blow} (Table 2). Most of the smaller grains move on unbound orbits
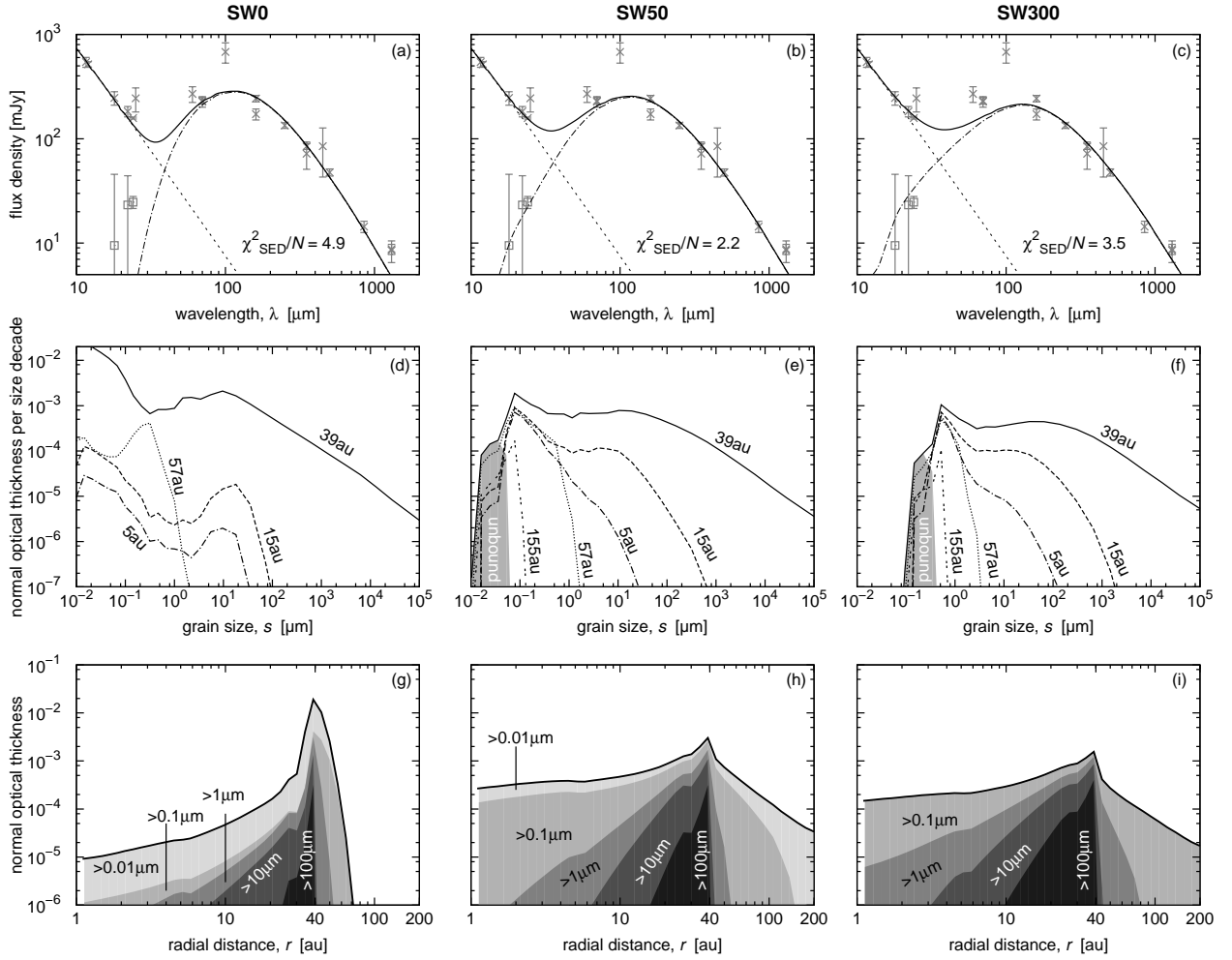
Fig. 2. Disc models of narrow planetesimal belts centred at 40 au with different assumptions for the stellar wind (SW) strength (*from left to right* $\dot{M}_\star = 0, 50, 300\ \dot{M}_\odot$). *(a) – (c):* SEDs. Crosses show photometric data and squares star-subtracted photometric data. The dashed lines depict the stellar photosphere, the dash-dotted lines the disc emission, and the solid lines the star+disc emission. The χ^2_{SED}/N were obtained using the $N = 20$ photometric points in the plotted range. *(d) – (f):* normal optical thickness as a function of grain size at different distances from the star. The solid curves ($r = 39$ au) show the particle distribution within the parent belt. Shaded regions depict the contribution of grains on unbound orbits at $r = 39$ au. *(g) – (i):* normal optical thickness as a function of distance from the star. Shaded regions mark the contributions from different size ranges.

and leave the system on short timescales. Towards larger grains, the size distributions in the parent belt are nearly flat until they become significantly steeper at sizes between 10 and 100 μm. This behaviour is caused by the strong transport due to stellar wind drag, which favours smaller particles and quickly removes them from the planetesimal ring (e.g., Vitense et al. 2010; Reidemeister et al. 2011; Wyatt et al. 2011; Krivov et al. 2013). As a result, the normal optical thickness is radially uniform for $r < r_{\mathrm{PB}}$ in SW50 and SW300 (Fig. 2h,i).

Direct stellar radiation pressure, aided by stellar wind pressure in SW50 and SW300, pushes submicron-sized, barely bound grains to eccentric orbits resulting in extended dust halos. However, both because of low dynamical excitation (Thébault & Wu 2008) and fast transport (Strubbe & Chiang 2006), the halos are tenuous and exhibit radial profiles with outer slopes that are significantly steeper than the -1.5 predicted for "canonical" debris discs (Krivov et al. 2006; Strubbe & Chiang 2006).

For all three runs, the surface mass density of solids, Σ, is rising with distance up to r_{PB} and shows a bow-like shape in a log-log $\Sigma - r$ diagram. Averaged over $r = 1 - 30$ au, we measured

$\Sigma \propto r^{2.0}$ for SW0, and $\Sigma \propto r^{2.7}$ for SW50 and SW300. The latter is close to $r^{2.8}$, derived by MacGregor et al. (2013). The dust mass (objects with radii up to $s = 1$ mm) is about $2 \times 10^{-3}\ M_\oplus$, consistent with previous estimates (Augereau & Beust 2006). The three models have a fractional luminosity of $4 - 5 \times 10^{-4}$, which is not far from 6×10^{-4} obtained by a modified blackbody fit (Liu et al. 2004).

Figure 3 shows the surface brightness profile extracted from the ALMA 1.3 mm image. The profile increases with distance up to ≈ 30 au and drops steeply beyond. Since long-wavelength observations reveal the spatial distribution of large particles that have similar orbital elements as the planetesimals, this break indicates the outer edge of a dust-producing planetesimal zone. For modelling of this profile, we assumed a disc inclination of $89.5°$ from face-on (Krist et al. 2005) and convolved the synthetic 1.3 mm images for SW0, SW50, and SW300 with the ALMA reconstructed dirty beam as produced by CASA after proper rotation. From these images, we extracted the radial profiles by integrating over a $0.1''$ central strip along the disc major axis. We allow for vertical scaling of the gathered synthetic profiles. The scaling factors account for an imperfect reproduc-
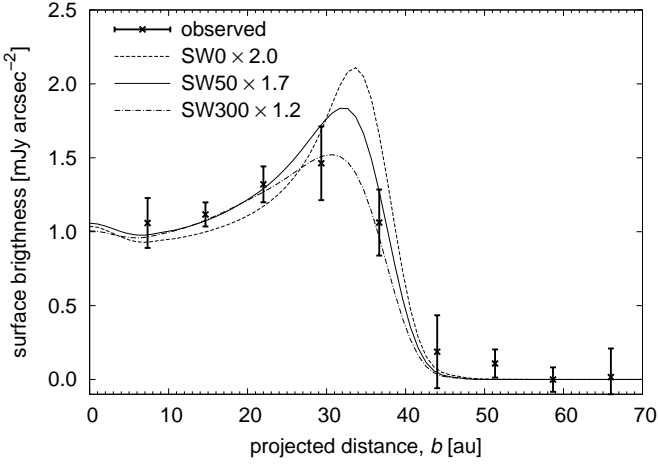
Fig. 3. ALMA radial surface brightness profile at 1.3 mm (dots) vs. models (lines). Synthetic profiles are multiplied by the factors given in the legend to compensate imperfections of the modelling procedure (explained in the text).

tion of the total flux density at 1.3 mm, visible by comparing the models with the observed SED. Such imperfections stem, e.g., from uncertainties in the absolute flux calibration or in the optical properties of the dust grains (Löhne et al. 2012). Further, they derive from a real inability of our models to reproduce the ALMA flux density along with the other photometric data. We surmise that the latter reason mainly causes the models to distinctly underestimate the ALMA flux density and necessitates high scaling factors (Fig. 2). In addition, the dust model used possibly underestimates the dust emissivity at mm wavelengths. Figure 3 clearly shows that the surface brightness peak moves to smaller projected distances with increasing stellar wind strength, reflecting the enhanced inward transport of particles.

4.1.2. Impact on scattered light

We calculated the surface brightness of scattered light for our models along the projected distance, b, in the disc midplane by

$$S(b) = L_\star \int \int \frac{\pi s^2 Q_{\mathrm{sca}} S_{11}(\phi) n(r, s)}{4\pi r^2} \, \mathrm{d}s \, \mathrm{d}l, \qquad (2)$$

where $L_\star$ is the luminosity of the star, $n(r, s)\mathrm{d}s$ the dust number density of grains with radii in $[s, s + \mathrm{d}s]$ at a distance r, and $l = \pm(r^2 - b^2)^{1/2}$ the line of sight. Q_{sca} and $S_{11}(\phi)$ are the scattering efficiency and the scattering phase function of the grains, respectively. The latter can be retrieved from the 4×4 Mueller matrix S_{ij} and is a function of the scattering angle $\phi = \arcsin(b/r)$. We used Mie theory to determine Q_{sca} and $S_{11}(\phi)$. The ACE simulations provided the dust number density.

To compare with the observed V- and H-band surface brightness profiles presented in Fitzgerald et al. (2007), we integrated $S(b)$ over the filter transmission curves of the HST Advanced Camera for Surveys F606W (central wavelength $\lambda_c = 0.59\,\mu m$, width $\Delta\lambda = 0.23\,\mu m$) and the Keck NIRC2 camera ($\lambda_c = 1.63\,\mu m$, $\Delta\lambda = 0.30\,\mu m$). The disc surface brightnesses were expressed relative to the star for which we found 8.55 mag in V-band and 4.84 mag in H-band with our photosphere model. To account for the extended halo of small particles, the flux was integrated up to stellocentric distances of $r = 150\,\mathrm{au}$ for each line of sight. We also compared with the radial profiles extracted from the high-resolution HST/STIS image by Schneider et al.

(2014). In their Fig. 39, the surface brightness is given for both sides of the disc along with their exponential fits. We averaged both fits and converted the flux from mJy/arcsec^2 to mag/arcsec^2 using the zero-point magnitude flux of 3671 Jy and then subtracted a stellar V-band brightness of 8.837 mag according to Table 1 in Schneider et al. (2014). The resulting V-band profile was found to be in good agreement with the Fitzgerald et al. (2007) data.

Figure 4 depicts the modelled and observed V- and H-band profiles as well as the disc colour, $V - H$. All models show significant deviations from the surface brightness data in both bands. Although roughly reproducing the observed slopes for $b < 40\,\mathrm{au}$, the synthetic profiles are steeper beyond, which is the halo zone, but get shallower with increasing stellar wind strength there. In terms of $V - H$, the SW0 and SW50 discs appear slightly blueish ($V - H < 0$), whereas the SW300 disc is red ($V - H > 0$), which completely disagrees with the observations. These effects are mainly due to the distribution and the amount of small grains in the disc. Increasing the stellar wind strength pushes more small particles in the halo zone (Fig. 2), and helps to enhance the scattered light flux beyond 40 au to approach the observed level. However, also the blowout size increases and the whole disc becomes more and more populated by larger particles that are stronger scatterers at longer wavelengths. Hence, the disc colour $V - H$ switches to red for too strong winds, clearly conflicting with the observational data.

Next, we considered the degree of linear polarisation, given by

$$P(b) = \frac{\int \int p(\phi) \, S_{11}(\phi) \, \pi s^2 Q_{\mathrm{sca}} \, n(r, s) \, \mathrm{d}s \, \mathrm{d}l}{\int \int S_{11}(\phi) \, \pi s^2 \, Q_{\mathrm{sca}} \, n(r, s) \, \mathrm{d}s \, \mathrm{d}l}, \qquad (3)$$

where $p(\phi)$ is the linear polarisation of a single particle. If $P(b)$ is positive (negative), the scattered light is partially polarised perpendicularly (parallel) to the scattering plane, i.e. the plane containing the star, the dust grains, and the observer.

As shown in Fig. 5, the observed monotonous increase of the degree of polarisation up to 80 au is roughly reproduced by SW50 only. In run SW300, the halo region is dominated by particles of $\approx 0.5\,\mu m$ in size which are about one order of magnitude larger than in SW50. Their polarisation $p(\phi)$ strongly oscillates with the scattering angle. Accordingly, the polarisation integrated over a range of scattering angles along the line of sights tends to average to small values and $P(b)$ does not rise with distance. For SW0, $P(b)$ increases up to the planetesimal belt as observed, but then decreases beyond.

Although SW50 fits the measured degree of polarisation best, the data are markedly overestimated by this model for $b < 40\,\mathrm{au}$. This is caused by particles dragged from the parent belt to the inner zone. Graham et al. (2007) and Fitzgerald et al. (2007) concluded that the inner disc region has to be relatively free of scattering grains, resulting in a low normal optical depth to scattering, $\tau_\perp^{\mathrm{sca}}(r) = \int \pi s^2 Q_{\mathrm{sca}} n(r, s) \, \mathrm{d}s$. In V-band, SW50 gives $\tau_\perp^{\mathrm{sca}}(r < r_{\mathrm{PB}})/\tau_\perp^{\mathrm{sca}}(r = r_{\mathrm{PB}}) \geq 0.1$, which is at least two orders of magnitude greater than the limit found by Graham et al. (2007) and Fitzgerald et al. (2007). However, owing to strong stellar winds, the inward transport of a significant amount of dust is a natural outcome in the dynamical evolution of the outer planetesimal belt. Even if planets exist at $r < r_{\mathrm{PB}}$, small particles come through, as only slower, bigger particles can be efficiently scattered by planets or get trapped in mean-motion resonances (e.g., Reidemeister et al. 2011; Shannon et al. 2015). It is important to note that the deviations of the model from the data may
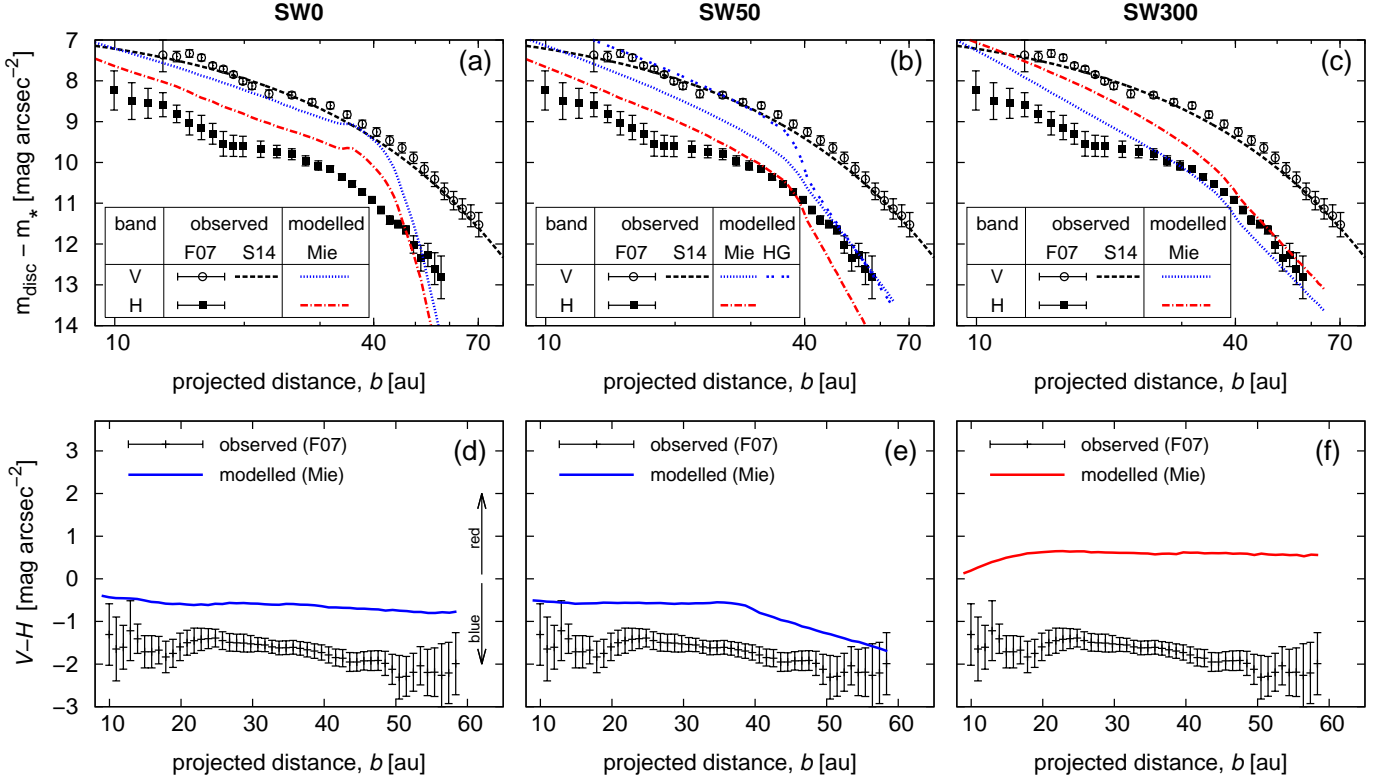
Fig. 4. Scattered light profiles of the AU Mic disc. *(a) – (c):* blue and red lines show synthetic midplane surface brightness profiles in *V*- and *H*-band relative to the stellar brightness for the disc models SW0, SW50, and SW300 (Sect. 4.1). Curves labelled with Mie in the legend were calculated with scattering phase functions obtained by means of Mie theory. The blue double-dotted line in panel *(b)* depicts the *V*-band profile generated with the best-fit Henyey-Greenstein (HG) phase function model of Graham et al. (2007). Dots represent measurements with 1σ errors from Fitzgerald et al. (2007), abbreviated as F07, averaged over the SE and NW wings (circles for *V*-band, squares for *H*-band). The black dashed line shows the averaged *V*-band fit to both wings obtained by Schneider et al. (2014), abbreviated as S14. *(d) – (f):* observed and modelled colour profiles, $V - H$, obtained with the F07 data and the Mie profiles shown in panels *(a) – (c)*.
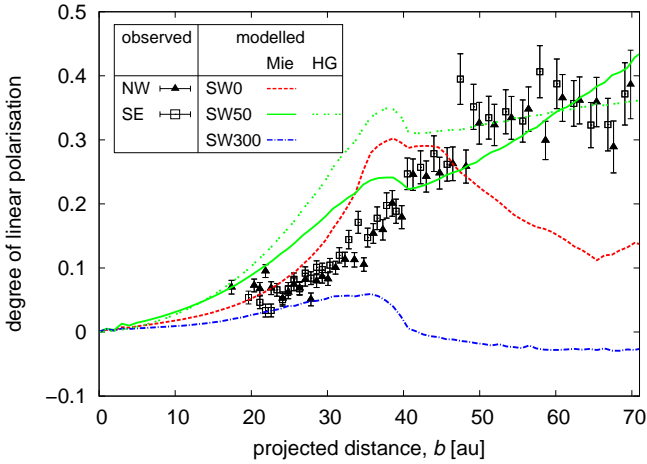
Fig. 5. Degree of polarisation as a function of projected distance. Squares and triangles are measurements for the SE and NW ansae, respectively (Graham et al. 2007). The double-dotted green line was obtained with the Henyey-Greenstein model of Graham et al. (2007), whereas the other lines are results from Mie theory.

be caused by the assumption of spherical dust grains. Real particle shapes significantly deviate from spheres because the bodies underwent a rich accretional and collisional history. While effective medium Mie spheres provide a good approximation to the total scattering cross sections of irregular particles, they cannot reproduce the scattering phase function and polarisation of such grains (Shen et al. 2008, 2009). Hence, Mie theory fails in reproducing the scattered light observations as it was recently shown for HR 4796 A (Milli et al. 2015; Perrin et al. 2015). In a study of the HD 181327 disc, Stark et al. (2014) also found an empirical scattering phase function, which is not fully reproducible with Mie theory, indicating strongly forward scattering grains. Thus, if the AU Mic disc is populated by similar particles, our models would poorly fit the scattered light measurements by using Mie theory.

In an additional test, we aim at illustrating the effect when deviating from the Mie sphere dust model. To this end, we adapted the Graham et al. (2007) best-fit Henyey-Greenstein (HG) model for $S_{11}(\phi)$ and $p(\phi)$, and re-computed the *V*-band surface brightness profile and the degree of polarisation for SW50 (double-dotted curves in Fig. 4b and Fig. 5). Note that $S_{11}(\phi)$ and $p(\phi)$ of the HG model are independent from grain size. Thus, all disc objects have the same scattering properties. The new synthetic *V*-band profile fits better the absolute values of the surface brightness flux for $b < 40$ au, whereas the de-

gree of polarisation rises too steeply in that range. Reasons for this behaviour can be identified by comparing $S_{11}(\phi)$ and $p(\phi)$ predicted by Mie theory and the HG model (Fig. 6). The HG phase function is distinctly broader than for Mie spheres with $s > 0.5\,\mu$m. That is why bigger particles can scatter more light towards the observer that leads to the V-band flux enhancement for $b < 40$ au as shown in Fig. 4b. Beyond 40 au, only small particles are present and the HG profile resembles the one of the Mie spheres.

However, the HG model shows strong deviations from the observed degree of polarisation, attributable to the form of the polarisation curve as a function of scattering angle (Fig. 6). The maximum of the polarisation occurs at $\phi_{\max} = 90°$, so that the main contribution to the polarised light comes from particles with distances from the star nearly equal to their projected distances ($r \approx b$). The $\phi_{\max}$ of the Mie sphere polarisation functions strongly vary with s. This agrees with the trends found for irregularly-shaped particles (Shen et al. 2009). With such shifts of $\phi_{\max}$ the polarised light at a certain b mainly originates from particles at $r > b$. Furthermore, irregular grains smaller than $0.1\,\mu$m tend to be weaker polarisers than Mie spheres in the same size range. Both may help to generate a shallower increase of the degree of polarisation with projected distance. Thus, the consideration of irregular particles in the scattered light analysis seems to be an attractive possibility to mitigate the deviations between the observed and modelled degree of polarisation.

We summarise that all our models have a large amount of small grains within the parent belt in contrast to what was found in previous studies and none of our models provides good fits to the scattered light data. There are two ways to interpret this result: (1) Our models may predict the actual dust distribution in the disc well but Mie theory is not valid to simulate the scattering properties of the grains. Then, our analysis show a preference towards a scattered light model where the grains are weaker polarisers than Mie spheres with polarisation maxima at scatter-

ing angles different from 90°. (2) Mie theory is an appropriate technique for the scattered light analysis but there are shortcomings with respect to the dust density derived in the collisional modelling. The truth may also be a combination of (1) and (2). A consideration of point (1) goes along with the simulation of the emission from irregular particles which is beyond the scope of this work. Thus in the following, we consider only point (2) in more detail. Since the scenario SW50 is found to be in best agreement with the data amongst the three stellar wind strengths tested, we consider SW50 a reference model, which is the starting point for further individual parameter variations influencing the dust distribution.

4.2. Material composition

The chemical composition of the AU Mic disc might be similar to discs around other BPMG stars because they have formed in the same molecular cloud from the same material and are coeval. However, the disc objects are heavily processed during the debris disc and preceding protoplanetary disc phases. Thus, their composition may depend on the mass and luminosity of the host star. Circumstellar dust compositions for some BMPG members have already been analysed previously. Smith et al. (2009) and Churcher et al. (2011) considered grains with a silicate core and a mantle of organic refractories for SED modelling in the η Tel and HD 191089 systems. They pointed out that particles with small silicate cores and a porosity of 20% (η Tel) and 60% (HD 191089) provide good fits to the observed excesses. A similar model that incorporates porous core-mantle silicate grains, additionally covered by ice in the outer region of the disc, also reproduces the β Pic observations (Pantin et al. 1997; Li & Greenberg 1998; Augereau et al. 2001). Lebreton et al. (2012) tested various chemical compositions for the debris around HD 181327. They found the SED to be mostly consistent with grains consisting of amorphous silicate and carbonaceous material with a dominant fraction of ice. In addition, the particles have to have a porosity of 65%.

The material composition affects the dust distribution and the SED by changing β and the dust temperature, T_d (e.g., Kirchschlager & Wolf 2013 for the influence of porosity on β and T_d). We now depart from the mixture M1, used in our reference run SW50, to assess whether other materials can be viable for the AU Mic system. We repeated the simulation with the compositions M2, M3, and M4 explained in Table 2, and investigated modifications to observables (Fig. 7).

The material M2 represents compact particles, composed of silicate and carbon. For these, we found a shift of the SED towards shorter wavelengths that deteriorates the fit in the submillimetre to radio range. In M3 and M4, we included water ice additionally. All constituents are present in equal volume fractions in M3, whereas the porosity and ice fraction are increased in M4. M3 is in fairly good agreement with the observed photometry, only tending to underestimate the near-IR excess. The icier and more porous M4 produces an SED whose peak position remains rather unchanged but increases and decreases more steeply. This narrower SED distinctly disagrees with the near-IR and submillimetre measurements.

No large differences in terms of the degree of polarisation are noticeable for M1, M2, and M3, whereas M4 markedly underestimates the data. The latter gives evidence that the material must not be too icy and porous. Note that modelling of the degree of polarisation is possibly affected by limitations of the Mie theory (see Sect. 4.1.2) that does not allow us to find strong constraints for the upper limit of the ice and vacuum content.
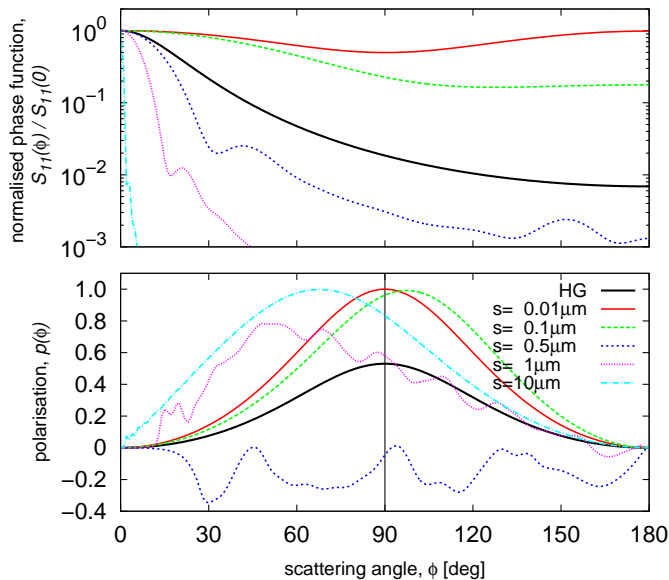

Fig. 6. Normalised scattering phase function (*top*) and polarisation (*bottom*) vs. scattering angle in V-band. Solid black lines have been inferred by Graham et al. (2007) via a Henyey-Greenstein model. The coloured lines are for Mie spheres with radii s, made of material M1.
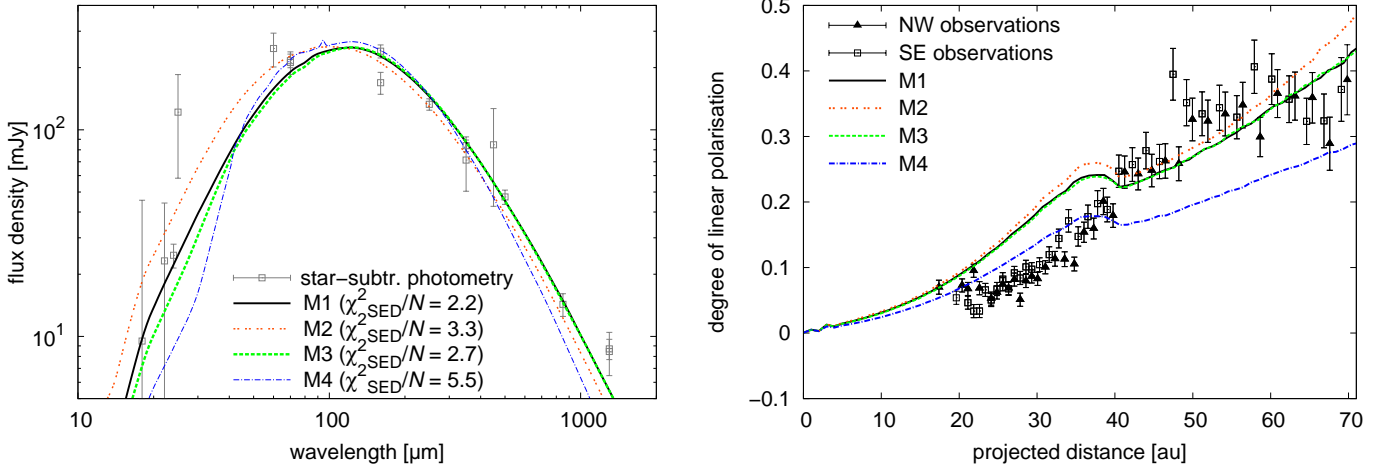
Fig. 7. Influence of the dust composition on the SED (*left*) and the degree of polarisation (*right*). The material names M1 – M4 are explained in Table 2. For better comparison of the SED models, χ^2_{SED}/N values are given.

We noticed little changes in the radial profile at $1.3\,\mathrm{mm}$ for all materials considered. This is caused by two characteristics of large grains, dominating the long-wavelength emission. First, large grains are weakly affected by stellar radiation and stellar winds and their spatial distribution is equal for different materials. Second, the dust temperature approaches the blackbody temperature with increasing particle size at a given distance (e.g., Fig. 5 of Pawellek et al. 2014). Therefore, T_d is nearly independent of the chemical composition for large grain sizes.

Altogether, the SED and the degree of polarisation seem to be consistent with materials having a small fraction of ice and a moderate porosity.

4.3. Dynamical planetesimal excitation

The maximum eccentricity of the planetesimals, e_{max}, represents the disc's dynamical excitation since this parameter affects the impact velocities of the objects, and therefore, the amount of small grains produced in collisions. In addition to the reference model with $e_{\mathrm{max}} = 0.03$, we consider $e_{\mathrm{max}} = 0.01$, a low value corresponding to the expected maximum level of pre-stirred discs (Matthews et al. 2014, and references therein), and $e_{\mathrm{max}} = 0.1$, a high value representing the dynamical excitation in

Fig. 8. SED models for different values of the maximum eccentricity, e_{max}, of the planetesimals orbits.

the Edgeworth-Kuiper belt (e.g., Vitense et al. 2010). The resulting SEDs are shown in Fig. 8.

Increasing e_{max} favours the production of small particles and shifts the SED maximum to shorter wavelengths. Thus, the model with $e_{\mathrm{max}} = 0.1$ well agrees with the excess data at $\lambda < 70\,\mu\mathrm{m}$, but completely fails to reproduce the ones at longer wavelengths. In contrast, $e_{\mathrm{max}} = 0.01$ provides a good match to the photometry beyond $100\,\mu\mathrm{m}$, but strongly deviates from the measurements at $\lambda \leq 70\,\mu\mathrm{m}$. Improvements may be possible by additional variations of other parameters. For instance, shifting the planetesimal belt inwards (outwards) increases (decreases) the dust temperature and helps to find a better SED fit for $e_{\mathrm{max}} = 0.01$ ($e_{\mathrm{max}} = 0.1$). However, any significant r_{PB}-shift would result in stronger deviations from the ALMA $1.3\,\mathrm{mm}$ profile, which constrains the location of a narrow planetesimal belt at around $40\,\mathrm{au}$. Another possibility would be broadening the SED towards shorter wavelengths for $e_{\mathrm{max}} = 0.01$. This can be achieved by stronger stellar winds as depicted in Fig. 2. However, stronger winds also lead to an increase of the blowout size, and therefore, it is more difficult to reproduce the observed blue disc colour (Sect. 4.1.2). Furthermore, other dust materials may have a positive effect on the SEDs. None of the materials investigated in Sect. 4.2 strengthens the submillimetre flux density, as required to improve the SED for $e_{\mathrm{max}} = 0.1$. Only one composition – the non-porous M2 material – predicts a stronger mid-IR emission from which the low-e_{max} model would benefit, but this material agrees less with the scattered light measurements. In summary, the reference run with $e_{\mathrm{max}} = 0.03$ matches the entire SED the best. Although values higher or lower than 0.03 seem to be unlikely, they cannot be ruled out completely if combined with other parameters, which was not explored here.

An observational constraint on the dynamical excitation can be put by the vertical thickness of the disc through the equilibrium condition $i = e/2$, where i and e are the orbital inclinations and eccentricities of the disc particles. Thus, measuring the disc's opening angle at long wavelengths hints at the maximum eccentricity of the planetesimals. However, the AU Mic disc is vertically unresolved in the SMA and ALMA images (Wilner et al. 2012; MacGregor et al. 2013), which gives only upper limits of the disc extent in this direction. We compared synthetic vertical profiles of our $e_{\mathrm{max}} = 0.1$ model with the ones extracted from the ALMA image. The modelled profiles are marginally consistent with the ALMA data, con-
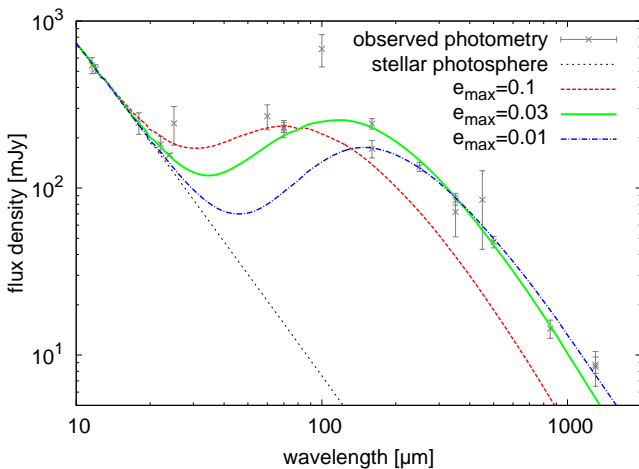
straining the disc's semi-opening angle to $i_{max} \lesssim e_{max}/2 = 0.05$. Interestingly, Krist et al. (2005) and Metchev et al. (2005) derived $i_{max} = 0.04 - 0.07$ from visible and near-IR images. Reading off the vertical scale height from the Schneider et al. (2014) high resolution STIS image gives $i_{max} = 0.03$. Thus, the observations yield a maximum eccentricity $e_{max} = 0.06 - 0.14$ that is excluded by our modelling. Resolving this contradiction may be possible if the vertical disc thickness seen in short-wavelength images does not necessarily points towards the dynamical state of the planetesimals. Thébault (2009) proposed a possibility for the AU Mic disc to develop a vertical thickness close to the observed value in the visible and near-IR although the disc is dynamically cold. In that model, the smallest grains have high in-plane velocities due to radiation and stellar wind pressure, and these velocities are partially converted into vertical ones in collisions with other particles. As a consequence, the disc becomes naturally thicker even without the gravitational perturbation of large, massive embedded bodies. In equilibrium, the disc has a large vertical dispersion of the smallest grains, whereas large particles remain close to the midplane. Thus, a low e_{max}, as preferred in our collisional modelling, can be consistent with the observed vertical disc thicknesses at short wavelengths.

4.4. Planetesimal belt width

4.4.1. 17 au-wide belt

As noted in Sect. 4.1.1, the outer edge of the planetesimal belt is well constrained by the ALMA profile. However, the edge-on orientation of the disc and the limited information on the innermost regions affected by the bright central source of unknown nature make the position of the inner edge of the disc, and so the disc extent, quite uncertain. In another test, we increased the planetesimal belt width from $\Delta r_{PB} = 5$ au (reference model) to $\Delta r_{PB} = 17$ au by shifting the inner edge to 25.5 au while keeping the outer edge at 42.5 au. The initial surface density was assumed to be constant over the belt width. Figure 9 compares the 17 au-wide belt scenario with the reference model.

The broader planetesimal belt has nearly the same SED as in the reference run and does not increase the warm emission although the dust production zone is more extended towards the star. The 1.3 mm profile of the 17 au-wide belt peaks closer to the star than for the reference model. Thus, it tends to underestimate the observed surface brightness farther out. This shortcoming does not hint at an implausibility of a broader planetesimal belt model since it can easily be compensated by shifting the outer edge from 42.5 au outwards. Although the broader belt scenario matches better the V-band profile than the reference run
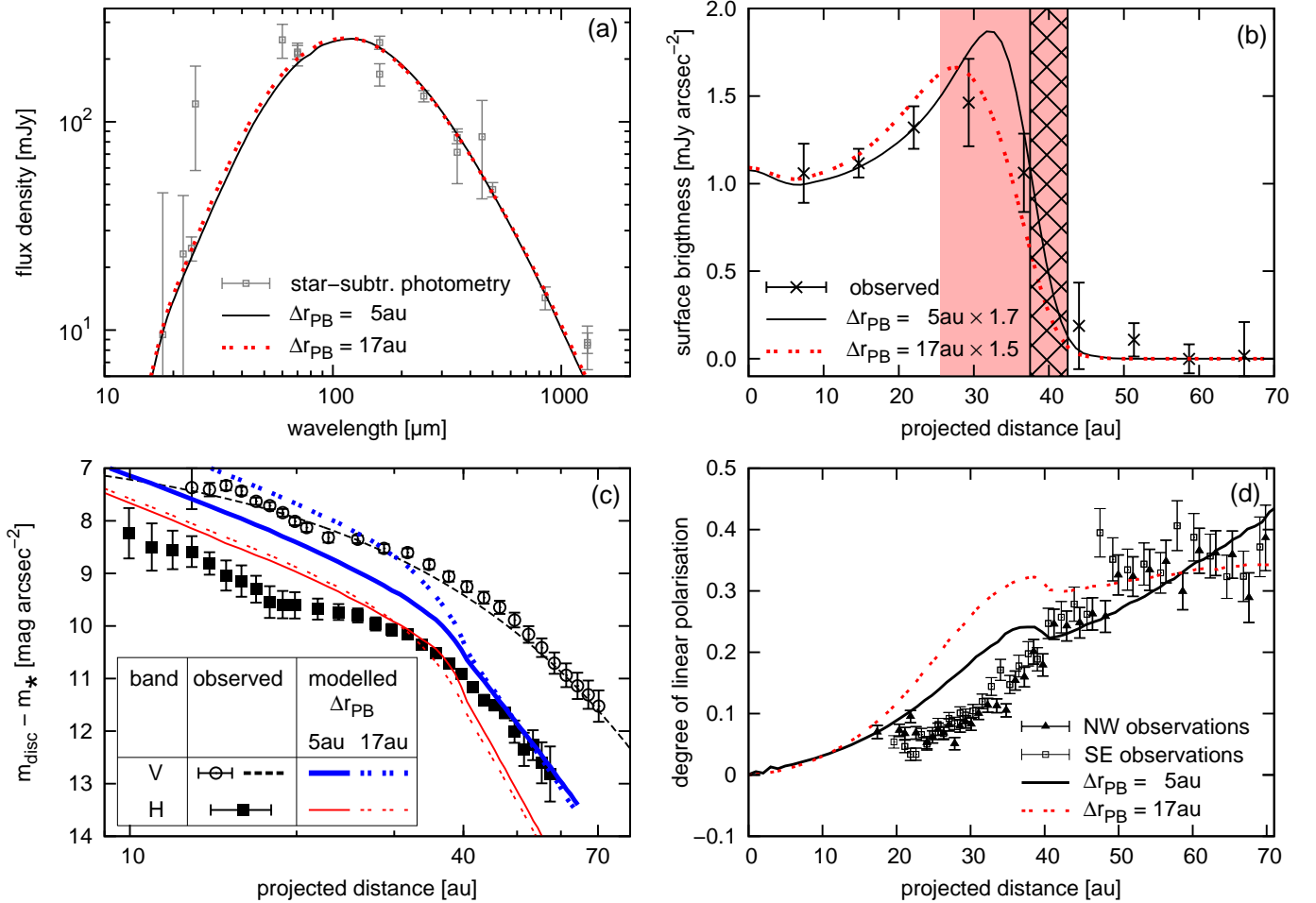

Fig. 9. Influence of the planetesimal belt width, Δr_{PB}, on *(a)* the SED, *(b)* the 1.3 mm radial profile, *(c)* the V- and H-band profiles, and *(d)* the degree of polarisation. The filled patterns in panel *(b)* depict the location and the radial width of the planetesimal belts (black-hatched 5 au, red-shaded 17 au). The profiles were vertically scaled by 1.7 ($\Delta r_{PB} = 5$ au) and 1.5 ($\Delta r_{PB} = 17$ au) to compensate the modelling imperfections mentioned in Sect. 4.1.1.
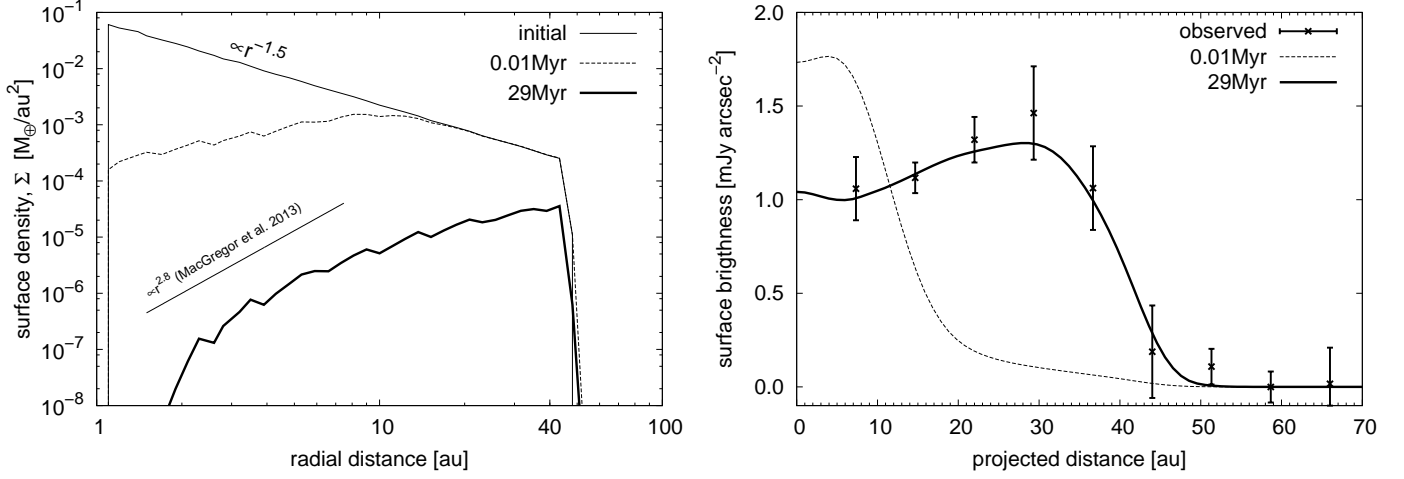
Fig. 10. *Left*: time evolution of the surface density in an extended planetesimal disc ($\Delta r_{PB} \approx 45$ au). The wavy structures of the Σ-curves are numerical artefacts. For the sake of comparison, the straight line shows the Σ-slope derived by MacGregor et al. (2013). *Right:* time evolution of the 1.3 mm profile along with the ALMA data. Note that the 0.01 Myr surface brightness profile was scaled by a factor of 0.05 for better visibility.

does, the degree of polarisation shows stronger deviations which may be attributed to the light scattering model (Sect. 4.1.2).

4.4.2. 44 au-wide belt

We now address the possibility that the AU Mic disc was populated by planetesimals over a wide range of distances. In such a disc, the innermost planetesimals have the shortest collisional lifetimes and are depleted within a few Myr, resulting in a surface density increasing outwards (Kennedy & Wyatt 2010). Due to the inside-out erosion of objects, an extended planetesimal disc may look like a narrow belt in long-wavelength observations, even if there are no planets within the disc that have swept up the inner region. In their study of the collisional evolution of a fiducial, 100 au-wide disc, Thébault & Augereau (2007) confirmed that the surface brightness peaks at (sub)millimetre wavelengths close to the outer edge of the planetesimal distribution after several Myr. Thus, the extended-disc scenario is an auspicious alternative for explaining the rising ALMA profile up to projected distances of ≈ 30 au in the AU Mic system. The significant fall beyond 30 au may mark the point beyond which planetesimals have not formed at all or where the disc was truncated.

To assess the feasibility of this scenario, we started an `ACE` simulation with a broad radial distribution of planetesimals from 1 to 45 au. Here we already accounted for a slight shift of the outer edge from the reference value 42.5 au to 45 au, as suggested in Sect. 4.4.1. The run was initialised with a solid surface density given by the Minimum Mass Solar Nebula (MMSN) model, $\Sigma \propto r^{-1.5}$. We considered bodies up to 100 m in radius and assumed pre-stirred planetesimals with $e_{max} = 0.03$ (Sect. 4.3).

Figure 10 depicts the evolution of the surface density and the 1.3 mm profile. The surface density quickly dropped close to the star due to particle erosion and the initially negative slope (-1.5) switched to a positive slope in a few ten thousand years. Note that the particles' collisional lifetimes were shorter than their orbital periods at the beginning of the simulation due to the large particle density at that phase. Thus, two consecutive collisions of one object are correlated and the orbit averaging method, implemented in `ACE`, is a crude approximation to determine the phase space density. Therefore, the results for the first

one hundred thousand years of simulation time should be treated with caution.

Owing to the progressive inside-out depletion of the planetesimals, the maximum of the 1.3 mm profile moved towards larger distances as time elapses. After 3 Myr, we noticed that the profile peak reached a maximum distance of about 30 au, which is in good agreement with the ALMA data. The absolute flux level of the observed dust emission was reproduced after 29 Myr. The final run fits the SED, the scattered light profiles, and the degree of polarisation with nearly the same fidelity as the 17 au-wide belt model (Sect. 4.4.1).

Note that the collisional evolution of the disc was artificially shortened as the largest bodies in the disc had been 100 m in size. If the disc is contains larger bodies, the inside-out planetesimal depletion is slower and the disc needs more time to reach the collisional equilibrium (Löhne et al. 2008). As a result, it takes longer than 3 Myr to reach the observed shape of the 1.3 mm profile. This way, scaling the model to the proper age of the system is possible. However, we refrained from further simulations, because of the numerical complexity of the extended planetesimal disc simulation[1]. The run presented does illustrate the feasibility of an extended planetesimal disc scenario sufficiently well.

5. Unresolved central emission

In Sect. 4, we did not care about the nature of the inner unresolved component and assumed its contribution to the flux densities at all wavelengths to be negligible. However, this may not be true if the unresolved central emission originates from an inner dust ring. The dust there would be much warmer than in the outer disc and would emit significantly at short wavelengths, while adding little flux in the mm range. We now consider the possibility of an additional inner planetesimal ring in the AU Mic system. If such a ring could exist, we should also investigate its consequences for the modelling of the resolved outer disc, discussed in Sect. 4.

A putative inner dust ring has to be 6 times brighter than the stellar photosphere at 1.3 mm (MacGregor et al. 2013, and Sect. 2.2 of this paper). Simultaneously, the ring has to emit

---

[1] It took about 150 CPU days to evolve the disc over 29 Myr.

weakly in the mid-IR in order not to contradict the measured excess there. Since an ALMA resolution of about 0.6" (≈ 6 au) was achieved, the ring should be located at distances $\lesssim 3$ au to be compatible with remaining unresolved. We placed an inner planetesimal ring at $r_{PB,in} = 3$ au, having a full width $\Delta r_{PB,in} = 0.4$ au, and assumed $e_{max} = 0.03$ and 50 times the solar wind strength. We made sure that the ring emission did not exceed the excess shortward of 24 μm and then investigated its emission at 1.3 mm. Figure 11 shows the results.
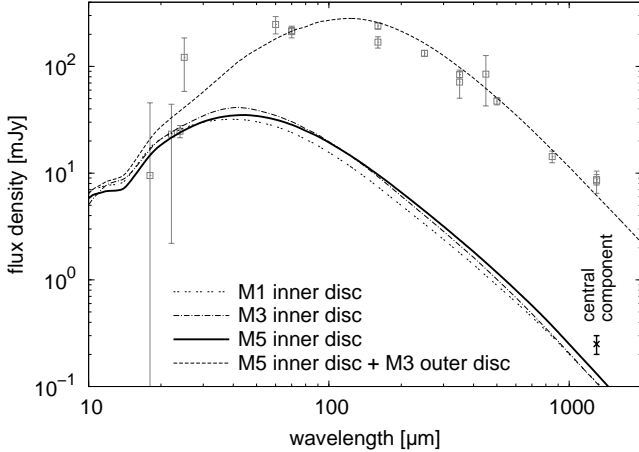
Fig. 11. SEDs of the inner planetesimal rings centred at $r_{PB,in} = 3$ au (width $\Delta r_{PB,in} = 0.4$ au) for the compositions M1, M3, and M5 (Table 2). Squares illustrate the photosphere subtracted photometry. The black cross in the right lower corner shows the emission of the unresolved star subtracted central component at 1.3 mm with 1σ uncertainty. The dashed line represents the M3 outer disc in Fig. 7 in combination with the inner M5 disc.

First, we assumed two inner rings with M1 and M3 – materials we found suitable for the outer component (Sect. 4.2). Consistency with the short-wavelength excess was achieved with a maximum dust mass of $\approx 5 \times 10^{-6}\ M_\oplus$. The rings are not bright enough to completely reproduce the central emission. Although M3 enhances the SED maximum, the long-wavelength slope is steeper and levels to nearly the same flux density at 1.3 mm as for M1. In another attempt, we considered highly porous grains (M5). This is motivated by the possibility that icy grains are produced beyond the ice line and then drift towards the star by drag forces. Accordingly, the particles get heated and their sublimated ice fractions are replaced by vacuum inclusions, which increase the porosity. Assuming an ice sublimation temperature $T_{subl} = 100$ K (e.g., Kobayashi et al. 2008) yields an iceline at $r_{ice} = (L_\star/L_\odot)^{0.5} (T_{subl}/277\,\text{K})^{-2}$ au ≈ 2 au, which is close to $r_{PB,in}$. The M5 material emits slightly more than M1 and M3 in the mm regime, but reproduces only about 60% of the observed central flux density. This constrains the maximum fraction of the central emission that can be explained by pure dust emission. Thus, the central emission must originate only or in parts from another source. Note that the star itself can contribute to the central emission, for instance due to an active stellar corona (Cranmer et al. 2013). Furthermore, stars may emit more flux at long wavelengths than predicted by the purely photospheric models for their spectral class. ALMA observations of the G- and K-type stars α Cen A and B show a flux enhancement by 20–30% in band 7 and almost doubling of the flux in band 3

(Liseau et al. 2015). Provided such a trend continues to an M dwarf like AU Mic, we do expect a significant stellar contribution to the observed central emission.

To get the total SED, the inner ring should be combined with an appropriate model for the outer disc. In order to avoid contradictions with the data, the outer disc has to emit less flux in the mid-IR where the SED of the inner ring peaks. This is well achieved by the M3 outer disc (Sect. 4.2), and indeed, in combination with the M5 inner ring the overall SED is well reproduced (Fig. 11, dashed line). Furthermore, a combination of the icy material in the outer ring and iceless, highly porous material in the inner ring is reasonable, as explained above. We adopted the outer disc SED from the model described in Sect. 4.2 without any adjustments (e.g., vertical scaling) that one possibly expects due to the presence of the inner ring. Thus, even if the inner emission stems from dust, it seems to barely affect the outer disc modelling. The χ^2_{SED}/N increases from 2.7 for the M3 outer disc to 3.3 for the combined M5 inner and M3 outer disc. The larger χ^2_{SED}/N is mostly due to the deviation of the inner+outer disc model from the *Spitzer*/MIPS 24 μm point. However, the overestimated flux density at 24 μm may be compensated by a modification of the dust composition. As seen in Fig. 7, adding ice reduces the flux in the mid-IR, while leaving it nearly unchanged at longer wavelengths. This promises improvements if a material icier than M3 for the outer disc is used. We highlight the small shift of the blowout size when going from iceless to icy grains (Tab. 2). Accordingly, the abundance of small grains will not change significantly, still reproducing the scattered light data (Sect. 4.1.2).

We stress that our two-component model does not account for the collisional interaction between inner and outer component which is mainly caused by two effects: (i) collisions of inner disc particles with inwards dragged grains from the outer disc and (ii) collisions between unbound particles produced in the inner ring with outer disc particles. By comparing the normal optical thicknesses of inner and outer component, including bound and unbound grains, we found $\tau_{\perp,out}/\tau_{\perp,in} \sim 0.1$ at 3 au and $\tau_{\perp,in}/\tau_{\perp,out} \sim 0.001$ at 40 au. Thus, collisional interaction between both is weak, justifying our modelling strategy.

6. Comparison with parametric modelling

Collisional modelling allows us to explore only a small number of parameter combinations. Although the models found reproduce the data satisfactorily, they are not unique, and better solutions may exist. In order to find an independent confirmation of the collisional modelling results, we additionally analysed the data with a multidimensional fitting approach. In that approach, the dust number density was assumed to be a combination of two independent power laws, representing the size and radial distribution of the grains. This model does not consider the physical mechanisms of the dust production and evolution. However, it is well suited for an exploration of a wide parameter space to find the most likely solutions that we compared with the collisional modelling results.

In the power-law model, the surface density follows r^α between the inner and outer cut-off radii, R_{in} and R_{out}, while the grain size distribution follows s^γ between the lower and upper cut-off grain sizes, s_{min} and s_{max}. The influence of s_{max} is negligible for reasonably steep grain size distributions with $\gamma < -3$. We fixed s_{max} to 2 mm. The dust mass M_d is an additional free parameter. The disc inclination was fixed to $\theta = 90°$. For the dust composition, we assumed compact, spherical grains composed of pure astronomical silicate (Draine 2003). This makes a total

Table 4. Power-law fitting results.

Parameter	Range explored	# values	Distr.	Best-fit [3σ]	+ inner
R_{in} [au]	2 – 60	187	temp	3.1* [2.0* – 24.8]	14.5
R_{out} [au]	3 – 100	155	temp	41.9 [37.3 – 45.5]	41.9
α	-5 – 5	101	lin	2.8 [1.8 – 4.8]	3.5
s_{min} [μm]	0.2 – 20	494	log	0.2* [0.2* – 0.5]	1.8
s_{max} [μm]	2000	1	fixed	…	…
γ	-5 – -3	21	lin	-3.3 [-3.4 – -3.3]	-3.3
θ	90°	1	fixed	…	…
M_d [$M_\oplus$]	…	…	cont	4.7×10^{-3}	5.7×10^{-3}

Notes. The distributions of the values considered in the parameter space are: *temp* – by equal steps in temperature of the grain size with the steepest radial temperature gradient, *lin* – linear, *log* – linear in the logarithm of the parameter, *fixed* – fixed value (no distribution at all), *cont* – continuous (scaling of the disc mass to minimise the χ^2 for given values of all other parameters). Values marked with * are at (or very close to) the boundaries of the parameter space explored and cannot be considered as reliable. The real values may lie outside the parameter space explored. The column "+ inner" shows best-fit values of the outer disc after subtracting a model of the inner, unresolved component, assuming it to be a debris disc. These values illustrate the uncertainties of the model parameters due to the unknown nature and uncertain parameters of this component. The mass values given are for grains up to $s = 1$ mm.

of eight free parameters, R_{in}, R_{out}, α, s_{min}, γ, M_d, the dust composition (sampled by only one value, namely 100% astronomical silicate), and the vertical scaling of the ALMA profile. For the fitting of the SED and the ALMA profile, we used the SAnD code (Ertel et al. 2012a; Löhne et al. 2012) which was originally developed for fitting simultaneously SED data and spatially resolved *Herschel* data as part of the *Herschel*/DUNES modelling tool box. Note that we did not include the scattered light data for this power-law fitting.

In a first approach, we fitted the model to the data ignoring the contribution of the central component. The best-fit model (Table 4) reveals features we already found, at least qualitatively, by collisional modelling: an outward-increasing surface density with an index close to 2.8, a well constrained outer disc radius at about 40 au, a small lower grain size < 1 μm consistent with a moderate level of stellar winds, and a relatively shallow slope of the grain size distribution, $\gamma = -3.3$, indicating that small particles are more affected by transport than collisions. Furthermore, the results are widely consistent with earlier studies of the disc (Augereau & Beust 2006; MacGregor et al. 2013).

In a second approach, we assumed the inner component to be an additional ring of dust. The ring was placed at 2 au from the star with an extent of 0.2 au and a constant surface density, which is just compatible with being mostly unresolved by the ALMA observations. The lower grain size, $s_{min,in}$, and the exponent, γ_{in}, of the size distribution for this inner component were explored by hand. The model was scaled to the flux density of the central component seen in the ALMA data. We found a very large lower grain size, $s_{min,in} = 5$ μm, as well as a very flat grain size distribution, $\gamma_{in} = -3$, to be necessary in order to keep the dust cold enough (the grains large enough) not to produce too much excess at mid- to far-IR wavelengths. It is important to note that this model serves to estimate the potential contribution of the unknown inner component, which is probably not a debris disc, to the SED. However, the fitting result, even the large lower grain size, might be consistent with a normal debris disc. A large $s_{min,in}$ is naturally expected if the grains do not experience a radiation pressure blowout limit as is the case for AU Mic. Then, the dominant or critical grain size, s_c, is the one where collisional and transport lifetimes are equal, which can be reached at much larger sizes. Including the effect of stellar wind drag in Eq. (6) of Kuchner & Stark (2010), and assuming an optical depth of

10^{-3} at 3 au in accordance with our M5 inner ring model, yields a critical size $s_c \approx 3$ μm, which is not far from $s_{min,in} = 5$ μm.

In a final step, we subtracted the contribution of the inner ring from the SED data and re-fitted the remaining flux by the two-power-law model used for our first approach (Table 4, last column). Comparing with the previous results illustrates the uncertainties of our first approach. The values are almost all within the 3σ-confidence interval of the first fit. This demonstrates that the inner component marginally influences the modelling of the resolved outer disc, as already found by collisional modelling.

7. Conclusions

We have performed in-depth collisional modelling of the AU Mic debris disc for the first time. A wealth of observational data have been considered, including the densely sampled spectral energy distribution, the ALMA 1.3 mm thermal emission profile, the scattered light profiles in *V*- and *H*-band, and the degree of scattered light polarisation as a function of projected distance in the disc midplane. Our study presents the first attempt to reproduce scattered light observations of a debris disc with collisional modelling.

Our models provide generic radial and size distributions of the particles in the whole disc. However, the disc also possesses several substructures and asymmetries like bumps and warps (Liu et al. 2004; Schneider et al. 2014) that may be caused by the perturbing effects of so far undetected planets. As our modelling technique is limited to axisymmetric discs, the formation of such disc properties was not considered in this work.

Most of the data can be reproduced with a narrow belt of planetesimals centred around 40 au with strong inward transport of dust by stellar winds, according to the birth-ring scenario of Strubbe & Chiang (2006). For modelling the ALMA 1.3 mm profile, a significant scaling factor $\lesssim 2$ was necessary. This mainly hints at the inability of our simulated dust distributions to fully reproduce the observed ALMA flux density. Additionally, the synthetic dust material used may underestimate the dust emissivity at mm wavelengths. We find a clear preference for a belt with a low dynamical excitation where the planetesimals orbits have a maximum eccentricity of 0.03. Our modelling allows us to make inferences on the stellar mass loss rate $\dot{M}_\star$, which is a measure for the stellar wind strength.

We can exclude extreme values of hundreds of the solar mass loss rate, $\dot{M}_\odot$, because these would cause strong deviations from the observed $V - H$ and the degree of linear polarisation. The best model was achieved with $\dot{M}_\star = 50\,\dot{M}_\odot$ that corresponds to the estimated wind strength during quiescent phases (Augereau & Beust 2006).

Due to strong dust transport from the planetesimal belt towards the star induced by the stellar wind drag, the inner disc region is filled with small scattering grains, contrary to what was derived previously (Graham et al. 2007; Fitzgerald et al. 2007). Significant deviations between the modelled and observed $V - H$ and the degree of linear polarisation are visible. The problem may be mitigated by irregularly-shaped grains that have scattering properties different from the Mie spheres used in this study. We find a preference for particles that are weaker polarisers than Mie spheres and have polarisation maxima at scattering angles different from $90°$. This again demonstrates the necessity to incorporate more realistic light scattering physics in simulations of resolved debris discs.

Our models support the presence of ice-containing particles of moderate porosity. As found by a comparison with other works, porous particles seem to be ubiquitous in discs around stars of the β Pic moving group.

The radial width of the plantesimal belt cannot be constrained tightly. Belts with radial extents of 5 and 17 au are consistent with the observations. Furthermore, we have addressed an alternative scenario with a very broad planetesimal belt, extended over $1 - 45$ au. The belt was assumed to be populated with particles up to 100 m in size and to have an MMSN-like surface density with initial radial index of -1.5. The inside-out evolution of this belt resulted in a rising surface density with distance from the star and a 1.3 mm profile as observed by ALMA. The scenario explains the formation of an outer ring-like planetesimal distribution and would be preferred if the presence of planets that cleared up the inner disc region are not confirmed in the future.

We have shown that the unresolved central emission at 1.3 mm, first reported by MacGregor et al. (2013), cannot stem from an inner dust ring alone. An inner ring located at $\lesssim 3$ au, which is compatible with being unresolved in the ALMA image, emits at most 60% of the observed central emission. We found a fractional luminosity ratio between inner and outer component of ≈ 0.4 – a typical value for a two-temperature disc system (Kennedy & Wyatt 2014). As suggested in MacGregor et al. (2013), future ALMA observations at higher resolution should be able to test the inner ring hypothesis. If confirmed, this might argue against the very extended belt scenario, based on the assumption that the inner planetesimals have not survived the inside-out collisional erosion of the disc. However, this assumption remains controversial because some models would explain the presence of an inner dust ring even after the collisional depletion of an extended outer ring. For example, the innermost particles of the extended planetesimal belt could be less icy, having a higher mechanical strength, and thus, would resist the collisional grinding more strongly. This increases the chance to detect leftover particles from the depleted, originally extended, planetesimal disc. Furthermore, cometary activity may play a crucial role to create hot dust in the inner disc zone. Altogether, because the central emission cannot be explained by dust emission alone, it fully or at least partly derives from the stellar chromosphere.

Our work provides a good indication of the probable generic architecture of the system, characterised by the spatial and size distributions of planetesimals and their collisionally-produced dust. All the models presented here are not unique as a full exploration of the parameter space by collisional modelling is impossible. However, we verified consistency of the collisional modelling results with a multidimensional power-law fitting approach for the radial and size distributions of the dust. This reduces the chance that our models show rather "exotic" solutions.

References

Augereau, J.-C. & Beust, H. 2006, A&A, 455, 987
Augereau, J. C., Nelson, R. P., Lagrange, A. M., Papaloizou, J. C. B., & Mouillet, D. 2001, A&A, 370, 447
Ballering, N. P., Rieke, G. H., Su, K. Y. L., & Montiel, E. 2013, ApJ, 775, 55
Beichman, C. A., Neugebauer, G., Habing, H. J., Clegg, P. E., & Chester, T. J., eds. 1988, Infrared astronomical satellite (IRAS) catalogs and atlases. Volume 1: Explanatory supplement, Vol. 1
Benz, W. & Asphaug, E. 1999, Icarus, 142, 5
Bertin, E. & Arnouts, S. 1996, A&AS, 117, 393
Binks, A. S. & Jeffries, R. D. 2014, MNRAS, 438, L11
Bohren, C. F. & Huffman, D. R. 1983, Absorption and scattering of light by small particles (New York: Wiley)
Bruggeman, D. A. G. 1935, Annalen der Physik, 416, 636
Burns, J. A., Lamy, P. L., & Soter, S. 1979, Icarus, 40, 1
Chen, C. H., Mittal, T., Kuchner, M., et al. 2014, ApJS, 211, 25
Chen, C. H., Patten, B. M., Werner, M. W., et al. 2005, ApJ, 634, 1372
Churcher, L., Wyatt, M., & Smith, R. 2011, MNRAS, 410, 2
Cranmer, S. R., Wilner, D. J., & MacGregor, M. A. 2013, ApJ, 772, 149
Cutri, R. M. & et al. 2012, VizieR Online Data Catalog, 2311, 0
Decin, G., Dominik, C., Waters, L. B. F. M., & Waelkens, C. 2003, ApJ, 598, 636
Doering, R. L., Meixner, M., Ardila, D., & Clampin, M. 2005, in Protostars and Planets V Posters, 8432
Draine, B. T. 2003, ApJ, 598, 1017
Eiroa, C., Marshall, J. P., Mora, A., et al. 2013, A&A, 555, A11
Ertel, S., Marshall, J. P., Augereau, J.-C., et al. 2014, A&A, 561, A114
Ertel, S., Wolf, S., Marshall, J. P., et al. 2012a, A&A, 541, A148
Ertel, S., Wolf, S., & Rodmann, J. 2012b, A&A, 544, A61
Fitzgerald, M. P., Kalas, P. G., Duchêne, G., Pinte, C., & Graham, J. R. 2007, ApJ, 670, 536
Forbrich, J., Lada, C. J., Muench, A. A., & Teixeira, P. S. 2008, ApJ, 687, 1107
France, K., Roberge, A., Lupu, R. E., Redfield, S., & Feldman, P. D. 2007, ApJ, 668, 1174
Gautier, III, T. N., Rieke, G. H., Stansberry, J., et al. 2007, ApJ, 667, 527
Graham, J. R., Kalas, P. G., & Matthews, B. C. 2007, ApJ, 654, 595
Griffin, M. J., Abergel, A., Abreu, A., et al. 2010, A&A, 518, L3
Gustafson, B. A. S. 1994, Annual Review of Earth and Planetary Sciences, 22, 553
Hebb, L., Petro, L., Ford, H. C., et al. 2007, MNRAS, 379, 63
Henyey, L. G. & Greenstein, J. L. 1941, ApJ, 93, 70
Houdebine, E. R. & Doyle, J. G. 1994, A&A, 289, 185
Ishihara, D., Onaka, T., Kataza, H., et al. 2010, A&A, 514, A1
Johnstone, C. P., Güdel, M., Brott, I., & Lüftinger, T. 2015a, A&A, 577, A28
Johnstone, C. P., Güdel, M., Lüftinger, T., Toth, G., & Brott, I. 2015b, A&A, 577, A27
Kains, N., Wyatt, M. C., & Greaves, J. S. 2011, MNRAS, 414, 2486
Kalas, P., Liu, M. C., & Matthews, B. C. 2004, Science, 303, 1990
Kennedy, G. M. & Wyatt, M. C. 2010, MNRAS, 405, 1253
Kennedy, G. M. & Wyatt, M. C. 2014, MNRAS, 444, 3164
Kirchschlager, F. & Wolf, S. 2013, A&A, 552, A54

Kobayashi, H., Watanabe, S.-i., Kimura, H., & Yamamoto, T. 2008, Icarus, 195, 871

Kral, Q., Thébault, P., Augereau, J.-C., Boccaletti, A., & Charnoz, S. 2015, A&A, 573, A39

Krist, J. E., Ardila, D. R., Golimowski, D. A., et al. 2005, AJ, 129, 1008

Krivov, A. V., Eiroa, C., Löhne, T., et al. 2013, ApJ, 772, 32

Krivov, A. V., Löhne, T., & Sremčević, M. 2006, A&A, 455, 509

Krivov, A. V., Müller, S., Löhne, T., & Mutschke, H. 2008, ApJ, 687, 608

Kuchner, M. J. & Stark, C. C. 2010, AJ, 140, 1007

Lada, C. J. 2006, ApJ, 640, L63

Lebreton, J., Augereau, J.-C., Thi, W.-F., et al. 2012, A&A, 539, A17

Lestrade, J.-F., Matthews, B. C., Sibthorpe, B., et al. 2012, A&A, 548, A86

Lestrade, J.-F., Wyatt, M. C., Bertoldi, F., Dent, W. R. F., & Menten, K. M. 2006, A&A, 460, 733

Lestrade, J.-F., Wyatt, M. C., Bertoldi, F., Menten, K. M., & Labaigt, G. 2009, A&A, 506, 1455

Li, A. & Greenberg, J. M. 1998, A&A, 331, 291

Liseau, R., Vlemmings, W., Bayo, A., et al. 2015, A&A, 573, L4

Liu, M. C. 2004, Science, 305, 1442

Liu, M. C., Matthews, B. C., Williams, J. P., & Kalas, P. G. 2004, ApJ, 608, 526

Löhne, T., Augereau, J.-C., Ertel, S., et al. 2012, A&A, 537, A110

Löhne, T., Krivov, A. V., & Rodmann, J. 2008, ApJ, 673, 1123

MacGregor, M. A., Wilner, D. J., Rosenfeld, K. A., et al. 2013, ApJ, 762, L21

Makarov, V. V. 2007, ApJS, 169, 105

Malo, L., Doyon, R., Feiden, G. A., et al. 2014, ApJ, 792, 37

Mamajek, E. E. & Bell, C. P. M. 2014, MNRAS, 445, 2169

Masciadri, E., Mundt, R., Henning, T., Alvarez\, C., & Barrado y Navascués, D. 2005, Mem. Soc. Astron. Italiana, 76, 416

Matthews, B. C., Krivov, A. V., Wyatt, M. C., Bryden, G., & Eiroa, C. 2014, in Protostars and Planets VI, ed. H. Beuther, R. Klessen, C. Dullemond, & T. Henning (Univ. of Arizona Press), in press

McMullin, J. P., Waters, B., Schiebel, D., Young, W., & Golap, K. 2007, in Astronomical Society of the Pacific Conference Series, Vol. 376, Astronomical Data Analysis Software and Systems XVI, ed. R. A. Shaw, F. Hill, & D. J. Bell, 127

Metchev, S. A., Eisner, J. A., Hillenbrand, L. A., & Wolf, S. 2005, ApJ, 622, 451

Milli, J., Mawet, D., Pinte, C., et al. 2015, A&A, 577, A57

Morales, F. Y., Rieke, G. H., Werner, M. W., et al. 2011, ApJ, 730, L29

Moshir, M., Kopan, G., Conrow, T., et al. 1990, in Bulletin of the American Astronomical Society, Vol. 22, Bulletin of the American Astronomical Society, 1325

Müller, S., Löhne, T., & Krivov, A. V. 2010, ApJ, 708, 1728

Nesvold, E. R. & Kuchner, M. J. 2015, ApJ, 798, 83

Neuhäuser, R., Guenther, E. W., Alves, J., et al. 2003, Astronomische Nachrichten, 324, 535

Ott, S. 2010, in ASP Conf. Series, Vol. 434, Astronomical Data Analysis Software and Systems XIX, ed. Y. Mizumoto, K.-I. Morita, & M. Ohishi, 139

Pagano, I., Linsky, J. L., Carkner, L., et al. 2000, ApJ, 532, 497

Pantin, E., Lagage, P. O., & Artymowicz, P. 1997, A&A, 327, 1123

Pawellek, N., Krivov, A. V., Marshall, J. P., et al. 2014, ApJ, 792, 65

Perrin, M. D., Duchene, G., Millar-Blanchaer, M., et al. 2015, ApJ, 799, 182

Perryman, M. A. C., Lindegren, L., Kovalevsky, J., et al. 1997, A&A, 323, L49

Pilbratt, G. L., Riedinger, J. R., Passvogel, T., et al. 2010, A&A, 518, L1

Plavchan, P., Jura, M., & Lipscy, S. J. 2005, ApJ, 631, 1161

Plavchan, P., Werner, M. W., Chen, C. H., et al. 2009, ApJ, 698, 1068

Poglitsch, A., Waelkens, C., Geis, N., et al. 2010, A&A, 518, L2

Rebull, L. M., Stapelfeldt, K. R., Werner, M. W., et al. 2008, ApJ, 681, 1484

Reidemeister, M., Krivov, A. V., Stark, C. C., et al. 2011, A&A, 527, A57

Roberge, A., Weinberger, A. J., Redfield, S., & Feldman, P. D. 2005, ApJ, 626, L105

Robinson, R. D., Linsky, J. L., Woodgate, B. E., & Timothy, J. G. 2001, ApJ, 554, 368

Schneider, G., Grady, C. A., Hines, D. C., et al. 2014, AJ, 148, 59

Schneider, P. C. & Schmitt, J. H. M. M. 2010, A&A, 516, A8

Schüppler, C., Löhne, T., Krivov, A. V., et al. 2014, A&A, 567, A127

Shannon, A., Mustill, A. J., & Wyatt, M. 2015, MNRAS, 448, 684

Shen, Y., Draine, B. T., & Johnson, E. T. 2008, ApJ, 689, 260

Shen, Y., Draine, B. T., & Johnson, E. T. 2009, ApJ, 696, 2126

Smith, R., Churcher, L. J., Wyatt, M. C., Moerchen, M. M., & Telesco, C. M. 2009, A&A, 493, 299

Stark, C. C., Schneider, G., Weinberger, A. J., et al. 2014, ApJ, 789, 58

Strubbe, L. E. & Chiang, E. I. 2006, ApJ, 648, 652

Su, K. Y. L., Rieke, G. H., Stansberry, J. A., et al. 2006, ApJ, 653, 675

Swinyard, B. M., Ade, P., Baluteau, J.-P., et al. 2010, A&A, 518, L4

Thébault, P. 2009, A&A, 505, 1269

Thébault, P. & Augereau, J.-C. 2007, A&A, 472, 169

Thébault, P. & Wu, Y. 2008, A&A, 481, 713

Theissen, C. A. & West, A. A. 2014, ApJ, 794, 146

Thureau, N. D., Greaves, J. S., Matthews, B. C., et al. 2014, MNRAS, 445, 2558

van Leeuwen, F. 2007, A&A, 474, 653

Vitense, C., Krivov, A. V., & Löhne, T. 2010, A&A, 520, A32

Wilner, D. J., Andrews, S. M., MacGregor, M. A., & Hughes, A. M. 2012, ApJ, 749, L27

Wright, E. L., Eisenhardt, P. R. M., Mainzer, A. K., et al. 2010, AJ, 140, 1868

Wyatt, M. C., Clarke, C. J., & Booth, M. 2011, Celestial Mechanics and Dynamical Astronomy, 111, 1

Wyatt, M. C., Smith, R., Su, K. Y. L., et al. 2007, ApJ, 663, 365

Zubko, V. G., Mennella, V., Colangeli, L., & Bussoletti, E. 1996, MNRAS, 282, 1321